First-principles study and mesoscopic modeling of two-dimensional spin and orbital fluctuations in FeSe

Abyay Ghosh [1], Piotr Chudzinski [1,2] and Myrta Grüning [1,3]

[1] *School of Mathematics and Physics, Queen's University Belfast, Belfast BT7 1NN, Northern Ireland, United Kingdom*

[2] *Institute of Fundamental Technological Research, Polish Academy of Sciences, Adolfa Pawińskiego 5b, 02-106 Warsaw, Poland*

[3] *European Theoretical Spectroscopy Facility (ETSF)*

(Received 19 March 2024; accepted 4 October 2024; published 18 November 2024)

We calculated the structural, electronic, and magnetic properties of FeSe within density-functional theory at the generalized gradient approximation level. First, we studied how the bandwidth of the d-bands at the Fermi energy is renormalized by adding simple corrections: Hubbard U, Hund's J, and by introducing long-range magnetic orders. We found that introducing either a striped or a staggered dimer antiferromagnetic order brings the bandwidths—which are starkly overestimated at the generalized gradient approximation level—closer to those experimentally observed. Second, for the ferromagnetic, the striped, checkerboard, and staggered dimer antiferromagnetic order, we investigate the change in magnetic formation energy with local magnetic moment of Fe at a pressure up to 6 GPa. The bilinear and biquadratic exchange energies are derived from the Heisenberg model and noncollinear first-principles calculations, respectively. We found a nontrivial behavior of the spin-exchange parameters on the magnetization, and we put forward a field-theory model that rationalizes these results in terms of two-dimensional spin and orbital fluctuations. The character of these fluctuations can be either that of a standard density wave or a topological vortex. Topological vortices can result in mesoscopic magnetization structures.

DOI: 10.1103/PhysRevResearch.6.043154

I. INTRODUCTION

The structurally simplest quasi-two-dimensional (2D) iron chalcogenide superconductor (ICS) FeSe [1] is of interest to the condensed-matter and materials physics community because of the unconventional superconductivity, the not yet understood origin of the nematic phase, and the absence of a long-range magnetic order [2–6]. The electronic structure and magnetic properties of the parent phase are investigated intensely, as they may help to explain those exotic properties.

FeSe presents a peculiar electronic structure, which it shares with other ICSs. The d_{xy} and $d_{xz/yz}$ orbital-derived bands around the Fermi level all contribute to the relevant physics of superconductivity, nematicity, and magnetism, for which ICSs are said to have a multiorbital multiband nature. This makes the use of effective models more difficult than for cuprates, for which a single-band effective model is sufficient. On the other hand, standard density functional theory (DFT) calculations are known to strongly overestimate—by nearly a factor 8 and 4, respectively [7]—the bandwidth of the relevant bands around the Fermi level when compared with angle-resolved photoemission spectroscopy (ARPES) experiments [7–9].

The renormalization of the conventional DFT bandwidth is the signature of correlation, which is missing at this level of theory. Calculations including strong local and long-range electron correlation at different levels of theory [10–16] [the addition of Hubbard's U, slave-boson theory, dynamical mean field theory (DMFT) either on top of conventional DFT, hybrid DFT, or quasiparticle GW] have been performed with partial success in reproducing the bandwidth of the relevant bands. A different approach has been taken in Ref. [17], which applied conventional DFT to a paramagnetic supercell [18] and found the bandwidth of the d_{xy} and $d_{xz/yz}$ bands to be strongly renormalized compared to nonmagnetic calculations, in quite good agreement with the ARPES results. Further, their effective band structure also reproduces the large broadening of the d_{xy} band around the Γ point. The latter work points to a strong interplay between electronic and magnetic properties and the need to consider the magnetic structure of FeSe to reproduce its electronic structure. Indeed, despite the absence of long-range magnetic order at ambient pressure, the consensus is that FeSe serves as a platform for diverse competing magnetic interactions such as Néel, stripe, or staggered-type antiferromagnetic interactions [19–22]. Applying hydrostatic pressure around 2 GPa induces stripe-type long-range order into the system [23]. Besides inducing long-range magnetic order into the system, the pressure-temperature phase diagram also reveals that pressure suppresses nematicity while superconducting T_c is enhanced by factor 4 [23,24]. Both spin and orbital degrees of freedom are supposed to play a key role in this phase diagram [25].

In this work, using DFT, we investigate the coupling of spin and orbital degrees of freedom, thus the interplay of electronic structure and magnetic properties of FeSe in its parent phase. Using field theory, we then consider the implications of such coupling, seeking to account for the missing correlation in standard DFT nonmagnetic calculations. This investigation is articulated in three parts.

In the *first* part (Sec. III), we systematically study how the electronic structure from conventional DFT, and specifically the bandwidths of the d_{xy} and $d_{xz/yz}$ orbital-derived bands, is modified when adding on-site magnetization, Hubbard U, and Hund's J. Remarkably, we find that a reasonable comparison with experimental data is obtained for phases hosting a magnetic order, either striped antiferromagnetic (SAFM) or staggered dimer (SD). This is in agreement with a finite on-site magnetization that minimizes the DFT energy. However, experiments do not support the existence of a macroscopic spin order at ambient pressure.

In the *second* part (Sec. IV), we compute within DFT the magnetic formation energy as a function of the local magnetic moment for varying pressure, thus we probe the energy landscape of different magnetic interactions. Since the local magnetic moment affects orbital occupation, these calculations provide insight into the role of the orbital degree of freedom, as highlighted in Refs. [26,27]. We map these results onto a Heisenberg-like Hamiltonian [28–30] to find a nontrivial dependence of the spin-exchange parameters on the local magnetic moments, which points to a strong coupling of the spin and orbital degrees of freedom.

The implications of this strong coupling are considered in the *third* part (Sec. V) at the many-body level, thus including collective phenomena, using field-theory modeling. We formulate a model that describes the spin and orbital collective fluctuations as two coupled 2D classical degrees of freedom, described by Kosterlitz-Thouless-type theories. Our model can capture highly nonlocal features, and in particular it can host mesoscopic patterns of orbital configurations, i.e., vortices in Kosterlitz-Thouless language. The motivation of our study, looking towards mesoscopic domains/patterns, comes also from recent experimental reports where nanoscopic Griffiths phases were found in FeSe [31]. We then demonstrate how the model accounts for the difference between the standard DFT nonmagnetic calculations and experimental observations.

II. COMPUTATIONAL DETAILS

The plane-wave pseudopotential suite QUANTUM ESPRESSO [32,33] is used to perform fully self-consistent DFT-based electronic structure calculations by solving the standard Kohn-Sham (KS) equations. Ultrasoft pseudopotentials from the PSlibrary [34] are used for Fe and Se atoms. Kinetic-energy cutoffs are fixed to 55 Ry for electronic wave functions after performing rigorous convergence tests.

The electronic exchange-correlation is treated under the generalized gradient approximation (GGA) that is parametrized by the Perdew-Burke-Ernzerhof (PBE) functional [35,36]. Hubbard's parameters used in the DFT + U calculations are determined from a piecewise linearity condition implemented through linear-response theory [37], based on density functional perturbation theory (DFPT) [38] as implemented in QUANTUM ESPRESSO. A dense q-mesh grid of $3 \times 3 \times 3$ is considered for the DFPT calculation. We have obtained a Hubbard U of 6.90 eV. This is larger than 4.06 eV previously obtained from the constrained random phase approximation [39,40].

A supercell of size $2 \times 2 \times 1$ is used to calculate magnetic moment-dependent energies in different magnetic phases like ferromagnetic (FM), checkerboard antiferromagnetic (CAFM), SAFM, and SD. In the CAFM phase, each spin is surrounded by four nearest neighbors (NNs) of opposite spins. In the SAFM phase, each spin is surrounded by two NNs of the same spins and two NNs of opposite spins. On the other hand, in the SD phase each spin is surrounded by one NN of the same spin and three NNs of opposite spins. We adopt the Monkhorst-Pack scheme [41] to sample the Brillouin zone in k-space with an $8 \times 8 \times 8$ grid. The band-unfolding technique as implemented in the BandUPpy module was used to get the primitive cell band structure from the supercell magnetic lattice [42–44]. The coordinates are optimized for each magnetic phase. Geometry optimization has been performed using the Broyden-Fletcher-Goldfarb-Shanno (BFGS) scheme [45]. The experimental lattice parameters (a, b = 3.7698 Å, c = 5.5163 Å, and $z_{\mathrm{Se}} = 0.2576$) are used as starting values. Convergence thresholds of 10^{-8} and 10^{-3} are used on total energy (a.u.) and forces (a.u.), respectively, for ionic minimization. High-pressure structures are obtained by enthalpy ($H = U + PV$) minimization under externally applied hydrostatic pressure. Fixed volume coordinate optimization calculation has been performed with long-range magnetic order at all pressures. The optimal magnetic moments are obtained from first-principles calculations with long-range magnetic order.

An energy penalty functional is used to perform the constrained magnetic moment calculations. The penalty term is incorporated into total energy by weight λ as $E_{\mathrm{total}} = E_{\mathrm{LSDA}} + \sum_i \lambda(M_i - M_i^0)^2$, where i is the atomic index for Fe atoms, and M_i^0, M_i are the targeted and actual local magnetic moment at atom i, respectively. The value of λ is fixed to 25 Ry/μ_B^2 after performing a convergence test, constraining the magnetic moment of Fe at a particular value. The angular dependence of energy is calculated by performing fully noncollinear first-principles calculations.

III. BANDWIDTH RENORMALIZATION

We present the results for the three t_{2g} orbital-derived bands d_{xy}, d_{xz}, d_{xy} which are dominant to the holelike bands crossing the Fermi level around the Γ point. We employ DFT (without and with spin polarization), DFT + U, DFT + J, both in the nonmagnetic (NM) case and assuming SAFM or SD order. We focus on the band dispersion, along the Γ-M direction, and we consider the difference between the maximum and the minimum band energy (see Fig. 8 and Appendix A), which in what follows we refer to simply as *bandwidth*. It has been observed from ARPES experiments that conventional nonmagnetic DFT strongly overestimates the bandwidth of both d_{xy} and $d_{xz/yz}$ bands. Here, we observe the effect of the on-site Hubbard repulsion, of Hund's J, which is predicted to play an important role for FeSe compounds [13,25],

TABLE I. Approximate values of bandwidth (in meV) along the Γ-M direction of the d_{xy}, d_{xz}, d_{xy} orbital derived bands at different levels of the theory and for different magnetic phases.

Nonmagnetic GGA/GGA+U				
Orbital	GGA	$U = 3.45$ eV	$U = 6.90$ eV	–
d_{xy}	834.8	698.5	565.8	–
$d_{xz/yz}$	572.8	632.2	681.1	–
Spin-polarized GGA/GGA+U				
Orbital	GGA	$U = 3.45$ eV	$U = 6.90$ eV	–
d_{xy}	645.1	579.8	160.7	–
$d_{xz/yz}$	436.5	468.0	995.3	–
Spin-polarized GGA+J				
Orbital	$J = 0.05$ eV	$J = 0.10$ eV	$J = 0.20$ eV	$J = 0.35$ eV
d_{xy}	621.7	600.6	555.4	454.0
$d_{xz/yz}$	429.5	426.0	415.5	398.1
Spin-polarized with long-range magnetic order				
Orbital	SAFM	$U = 1.0$ eV	$U = 2.0$ eV	$U = 3.4$ eV
d_{xy}	227.8	202.9	238.9	430.2
$d_{xz/yz}$	271.1	476.4	551.7	636.1
Orbital	$J = 0.05$ eV	$J = 0.10$ eV	$J = 0.20$ eV	$J = 0.50$ eV
d_{xy}	272.1	303.8	447.8	712.9
$d_{xz/yz}$	256.7	274.2	274.6	356.4

and SAFM and SD order. Though FeSe does not present a long-range magnetic order—contrary to ICSs, which mostly order magnetically—the SAFM has been observed to be the dominant magnetic fluctuation in FeSe [20], and SAFM order appears in the system at higher pressures [24]. We also considered the SD phase, which has been predicted theoretically to be slightly lower in energy than SAFM [46]. The results of the bandwidthof the t_{2g} orbital-derived bands are summarized in Table I.

NM GGA and GGA + U. The values calculated at the NM GGA level, 834.8 meV, and 572.8 meV for d_{xy} and $d_{xz/yz}$, respectively, are in agreement with [7]. As already reported [8], the bandwidths of these bands are strongly overestimated compared to experiments. Next, we add Hubbard U correlation, using for U both the value determined from DFPT and half of such a value, to study the dependence of the bandwidthon U. The determined U value for FeSe within DFPT stands at 6.90 eV, surpassing the 4.06 eV derived from the constrained random phase approximation [39,40]. The effect of U is strongly orbital-dependent: by increasing U, the bandwidthof d_{xy} decreases, whereas that of $d_{xz/yz}$ increases compared to NM GGA. This is consistent with previous LDA + U calculation [11]. The simple mean-field U correction is insufficient, as may be expected due to the multiorbital, multiband nature of the system.

Spin-polarized GGA and GGA + U. By just considering spin polarization, the bandwidthof NM GGA is renormalized by about a factor 1.3. As in the NM case, U is orbital-selective. The bandwidthof the d_{xy} derived band is renormalized to 160.7 meV at $U = 6.90$ eV, while the bandwidthof $d_{xz/yz}$ increases to the value of 995.3 meV.

Spin-polarized GGA + J: Adding increasing Hund's J shows a renormalization of the bandwidthof the t_{2g} orbital-derived bands. At $J = 0.35$ eV, the bandwidthof d_{xy} and $d_{xz/yz}$ is reduced to 454.0 and 398.1 meV, respectively. However, when further increasing J, the nature of the bands changes, bringing the calculated band structure in qualitative disagreement with the experimental observations. The combined addition of Hubbard U and Hund's J (results not shown) does not bring any improvement in applying the correction separately.

Long-range magnetic order GGA, GGA + U, GGA + J: The bandwidths of both d_{xy} and $d_{xz/yz}$ orbitals are renormalized to 272.1 and 256.7 meV, respectively, in SAFM phase. As previously observed, the addition of U is orbital-selective, at least in the case of "small" U. For $U = 1$ eV, the bandwidthof d_{xy} decreases to 202.9 eV and the $d_{xz/yz}$ bandwidthincreases to 476.4 eV. Instead, larger values of U in combination with magnetic ordering cause an increase of the bandwidthof both orbitals. The addition of a small Hund's J (0.05 eV) increases the bandwidthof d_{xy} slightly to 271.1 meV and decreases that of $d_{xz/yz}$ to 256.7 meV. As for the Hubbard parameters, larger values of J in combination with magnetic ordering cause an increase of the bandwidthof both orbitals. These results indicate that considering the magnetic ordering also accounts for most of the effects of adding the Hubbard U and Hund's J.

TABLE II. Bandwidth (in meV) calculated within DFT assuming either SAFM and SD long-range magnetic orders, compared with theoretical (DFT+DMFT) and experimental values from the literature.

Orbital	DFT+DMFT[a]	DFT@SAFM	DFT@SD	Expt.[b]
d_{xy}	225.0	227.8	169.8	37.5
$d_{xz/yz}$	200.0	271.1	367.8	155.0

[a]Reference [12].
[b]References [8,9].

Table II compares the bandwidthwe calculated within the GGA in the SAFM and SD long-range magnetic order, with those obtained from DFT + DMFT [12] and experimentally observed values. The bandwidthof d_{xy} obtained from DFT + DMFT is 225.0 meV, very close to the value 227.8 meV we obtained assuming a SAFM magnetic order. The bandwidthis further reduced to 169.8 meV by assuming the SD magnetic order. All these values are still too large by a factor 4–6 compared with the value of 37.5 meV extracted from experiments [8,9].

The calculated bandwidth of the $d_{xz/yz}$ band is 200.0, 271.1, and 367.8 meV for DFT + DMFT and assuming a SAFM and SD magnetic order, respectively. This is closer to the value extracted from the experiment, which is about 155.0 meV. Then, assuming a long-range magnetic order has a similar effect to introducing strong electron correlation through DMFT. Both DFT + DMFT and DFT with long-range magnetic order predict the bandwidthof the d_{xy} and $d_{xz/yz}$ orbital-derived bands to be of the same order, thus overestimating by a factor 4–6 the bandwidthof the d_{xy} band.

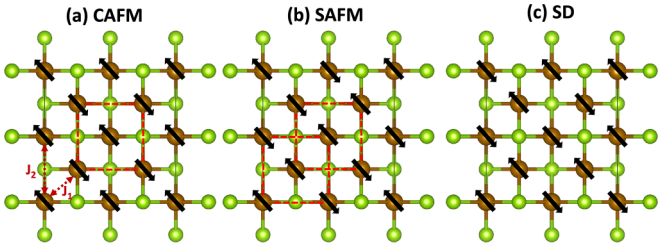

FIG. 1. Spin arrangement in FeSe magnetic lattice: (a) CAFM, (b) SAFM, and (c) SD. The brown and green dots represent Fe and As atoms, respectively. The black arrows in the lattice represent up and down spin. The red dashed lines highlight the AFM square (sub)lattice. The SAFM phase can be imagined as two interpenetrating AFM square sublattices. J_1 and J_2 are the NN and NNN spin-exchange parameters in the Heisenberg model (see Sec. IV B). The figure has been prepared using crystal visualization software VESTA [47].

IV. MAGNETIC PROPERTIES

We consider four different magnetic phases: FM, CAFM, SAFM, and SD. The three antiferromagnetic (AFM) configurations are shown in Figs. 1(a)–1(c). In the checkerboard phase [Fig. 1(a)], the NN spins are antiparallel to each other. In the striped phase [Fig. 1(b)], sites with the same spin form a stripe between stripes of opposite spin so that the next-nearest-neighbor (NNN) spins are antiparallel. In the staggered dimer phase, as the name suggests, sites with the same spin form dimers, and NN dimers have opposite spins. For each phase, at different hydrostatic pressures, we calculate the dependence of magnetic formation energy on the local magnetic moment (Sec. IV A). With such calculations, one can probe the magnetic phase in a high-spin or low-spin state and identify possible metastable states within the subspace of a given constrained magnetic moment. Then, we map these results into a Heisenberg model (Sec. IV B) and study the dependence of the spin-exchange parameters on the local magnetic moment at different hydrostatic pressures. Since changing the local magnetic moment corresponds to changing the orbital configuration, these calculations allow us to investigate the coupling of the orbital and spin degrees of freedom. Finally, we inspect the density of states (DOS) close to the Fermi energy (Sec. IV C).

A. Magnetic formation energy dependence on magnetization

The magnetic formation energy, ΔE, of a magnetic phase is defined as the energy difference per atom between the system in the magnetic phase (at a magnetic moment M) and the nonmagnetic phase. A magnetic phase is energetically favorable when $\Delta E < 0$. In Fig. 2, we plot the magnetic formation energy, ΔE, against the magnetic moment M at different values of the applied pressure for the magnetic phases considered. In the following discussion, we distinguish a low ($0.2\,\mu_B \leqslant M \leqslant 0.6\,\mu_B$), intermediate ($0.6\,\mu_B \leqslant M \leqslant 1.4\,\mu_B$), and high ($1.4\,\mu_B \leqslant M \leqslant 3.0\,\mu_B$) magnetization region. Similar to these regions, we also refer to low-spin (LS) and high-spin (HS) states because low values of Fe local magnetization correspond to a low-spin state configuration of the Fe atom, whereas high values

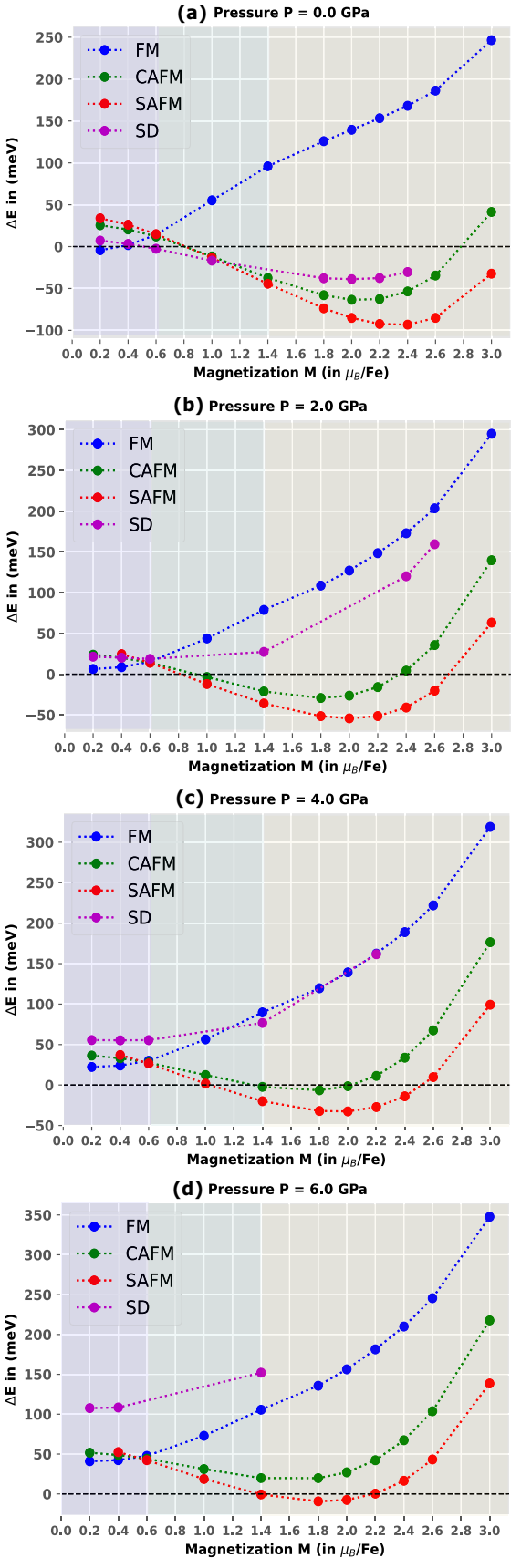

FIG. 2. Dependence of the magnetic formation energy with the local magnetic moment in (a) at ambient pressure (P), and with pressure (b) $P = 2.0$ GPa, (c) $P = 4.0$ GPa, and (d) $P = 6.0$ GPa.

of Fe local magnetization correspond to a high-spin state configuration.

At ambient pressure [Fig. 2(a)], in the LS state, the FM and the SD phases are the competing stable phases. At $M = 0.2\,\mu_B$, the FM phase is the only (slightly) energetically favorable phase ($\Delta E = -4.32$ meV). As the local magnetic moment increases, at $M \gtrapprox 0.4\,\mu_B$, a magnetic transition from FM to SD occurs: the SD phase becomes stable, while the FM phase becomes unstable. Between $1.0\,\mu_B$ and $1.2\,\mu_B$, the other AFM phases become stable and the three AFM phases are nearly degenerate. In the HS state, the AFM phases are stable (up to $2.8\,\mu_B$) and reach their minimum. The energy minima for SD ($\Delta E = -45.72$ meV) and CAFM ($\Delta E = -63.5$ meV) are found for a magnetization around $2.0\,\mu_B$. SAFM is the most stable with $\Delta E = -93.2$ meV around a magnetization of $2.3\,\mu_B$. As these energies are much larger in absolute value than superconducting transition temperature [1] (or even room temperature), these calculations predict that these magnetic phases should be thermally stable. In contrast, the experimental phase diagram of FeSe at ambient pressure shows no long-range magnetic order phases, although fluctuations—both of SAFM at $(\pi,0)$ and CAFM at (π,π)—have been observed in neutron scattering measurements over a wide energy range [20]. Also, the observed magnetic moment in the experiment is $2.28\,\mu_B$, which is close to the optimal magnetic moment of Fe we predict in the SAFM phase. The relative stability of the phases is similar to that obtained from calculations on the FeSe monolayer [48].

At a pressure $P = 2.0$ GPa [Fig. 2(b)], the FM and SD are unstable at all values of magnetization. Thus, no stable phases are observed at low spin (though we did not include spin-orbit coupling, which can potentially stabilize the FM or SD phase). The magnetic formation energy minima of the CAFM and SAFM are reduced in absolute value ($\Delta E = -29.2$ and -54.1 meV, respectively). According to these calculations then, the SAFM phase should be stable, in agreement with what was observed experimentally [23] at low temperatures. Also, the CAFM fluctuations should thus still be observable at this pressure. Furthermore, the reduced energy difference between CAFM and SAFM can allow spin-flip processes between these two phases.

As the pressure is increased to 4.0 GPa [Fig. 2(c)], the absolute values of the magnetization formation energy of CAFM and SAFM are reduced further to $\Delta E = -6.4$ and -32.6 meV. At pressure 6.0 GPa, the CAFM phase is unstable throughout the range of magnetic moment [Fig. 2(d)]. The majority of the striped fluctuations are eliminated and the energy minimum is shifted to $\Delta E = -9.3$ meV. Consequently, in agreement with experiments, long-range magnetic order disappears at about 6.0 GPa. Table III shows how the optimal value of the magnetic moment in the CAFM and SAFM phases decreases with increasing pressure.

TABLE III. Calculated optimal local magnetic moment of Fe (in μ_B) for the CAFM and SAFM phases for increased applied hydrostatic pressure. Here, optimal magnetization is the magnetization corresponding to the minimum value of the magnetization formation energy for the given phase. For increasing pressure, the optimal local magnetic moment of Fe decreases for both phases.

Pressure (GPa)	CAFM	SAFM
0.0	2.08	2.32
2.0	1.78	1.99
4.0	1.70	1.91
6.0	1.60	1.83

B. Heisenberg model Hamiltonian

We map the total energies for the considered phases into a Heisenberg-like model including nonlinear terms:

$$H = J_1 \sum_{ij}^{\mathrm{NN}} \vec{S}_i \cdot \vec{S}_j + J_2 \sum_{ij}^{\mathrm{NNN}} \vec{S}_i \cdot \vec{S}_j - K \sum_{ij}^{\mathrm{NN}} (\vec{S}_i \cdot \vec{S}_j)^2, \quad (1)$$

where J_1, J_2, and K represent NN, NNN, and biquadratic exchange interaction parameters, respectively. $\vec{S}_i$, $\vec{S}_j$ are spin magnetic moment at sites i and j, respectively. AFM (FM) states are defined by positive (negative) J_1, J_2. We choose not to include the third-nearest-neighbor term J_3 since it was found to be significantly smaller than J_1 (J_2 or K) for FeSe [30]. On the other hand, the biquadratic term is needed to capture the SD magnetic order (that from Fig. 2 is stable at ambient pressure) and in general the presence of higher-order magnetic fluctuations. In fact, this term has been recognized to be fundamental in modeling magnetic interactions and spin fluctuations in iron superconductors [28].

The NN and NNN exchange parameters, J_1, J_2, are calculated directly from the energies in Sec. IV A: we obtained J_1 by the difference between the energies of the FM and CAFM phases and J_2 by the difference between the energies of the SAFM and CAFM phases. The biquadratic term, K, is calculated [19,28] from a series of noncollinear total energy calculations performed by varying the angle, θ, between the two magnetic interpenetrating sublattices in the SAFM phase shown in Fig. 1(b) (see also Fig. 1 of Ref. [28]). The K parameter is then extracted by fitting the angular energy dependence $E(\theta)$ (see Appendix D for details) with

$$E(\theta) - E(0) = 2K \sin^2 \theta. \quad (2)$$

Figure 3 presents the dependence of the spin-exchange parameters on the magnetic moment at different applied hydrostatic pressures [49]. Table IV summarizes the results for

TABLE IV. Calculated exchange energy parameters [J_1, J_2, K in Eq. (1)] at optimal magnetization (corresponding to HS state) and at $M = 1.0\,\mu_B$ (corresponding to LS state). Here, optimal magnetization is the magnetization corresponding to the minimum value of the magnetization formation energy for all the considered phases. The ratios J_2/J_1 and K/J_1 are also reported.

P (GPa)	M (μ_B)	J_1 (meV)	J_2 (meV)	K (meV)	J_2/J_1	K/J_1
0.0	2.3	110.82	60.37	34.66	0.54	0.31
2.0	2.0	76.70	41.83	31.88	0.55	0.41
4.0	1.9	70.30	39.04	28.67	0.55	0.40
6.0	1.8	57.94	32.61	25.25	0.56	0.43
0.0	1.0	33.42	16.92	16.99	0.51	0.51
2.0	1.0	23.66	12.91	14.71	0.55	0.62
4.0	1.0	22.02	12.34	13.66	0.56	0.62
6.0	1.0	20.84	11.98	12.54	0.57	0.60

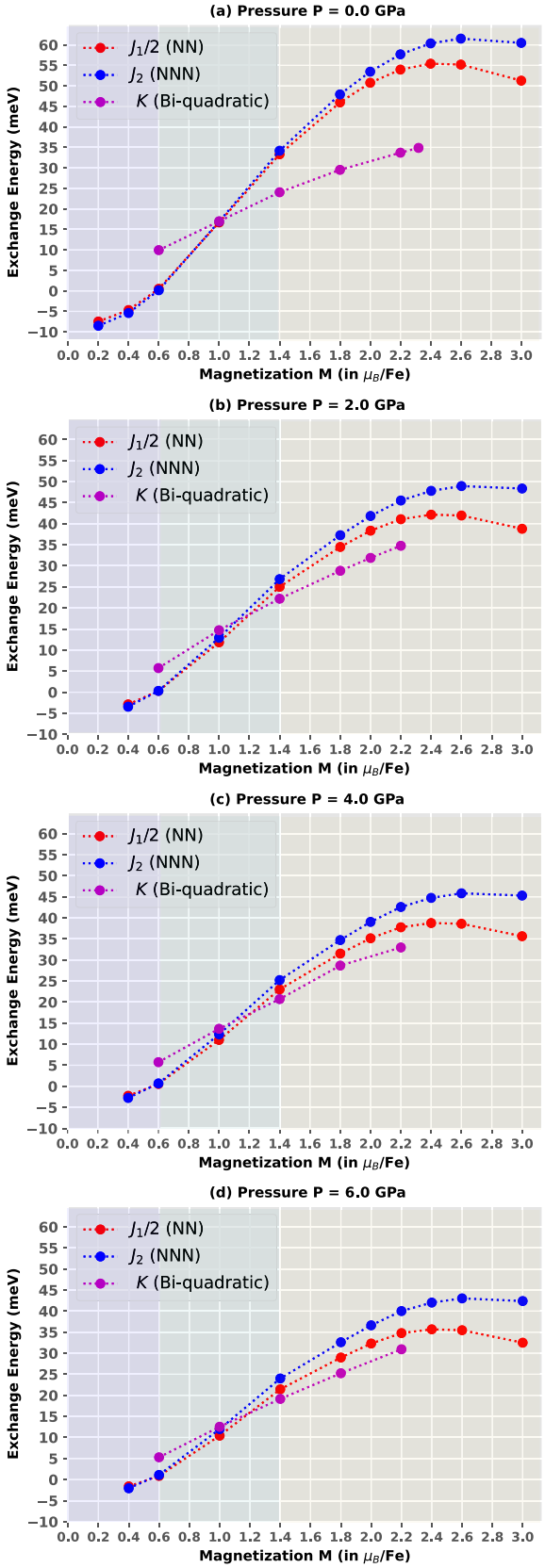

FIG. 3. Dependence on magnetic moment (M) of the spin-exchange parameters J_1, J_2, and K of the Heisenberg-like Hamiltonian in Eq. (1) calculated for different applied hydrostatic pressure P (a) at ambient pressure ($P = 0$), (b) $P = 2$ GPa, (c) $P = 4$ GPa, and (d) $P = 6$ GPa. The values of J_1, J_2 are multiplied by M^2.

two values of the magnetization: the optimal magnetization—defined as the magnetization corresponding to the minimum value of the magnetization formation energy for all the considered phases—and $M = 1.0\,\mu_B$—the magnetization close to which in Fig. 3(a), $J_1/2 \sim J_2 \sim K$.

For all pressures, $J_1/2$ and J_2 change from negative to positive when $M \gtrsim 0.6\,\mu_B$ (Fig. 3). This corresponds to what is observed in Fig. 2, where the FM phase is the most favorable in the LS state and AFM phases for the intermediate and HS state. For ambient pressure, this is consistent with an FM to AFM transition (in the SD configuration) as seen in Fig. 2, while at higher pressure all phases are unstable in the LS state. $J_1/2$ and J_2 have the same behavior and take similar values for the observed range of magnetization, being nearly degenerate for intermediate magnetization values around $M = 1.0\,\mu_B$ (see also Table IV). This corresponds to the near degeneracy of the CAFM and SAFM phases (and SD at ambient pressure) in Fig. 2. By increasing the pressure, the range of values that $J_1/2$, J_2 takes when varying the magnetization is reduced. The region where they are nearly degenerate is also reduced.

At the optimal magnetization (HS state), K (Table IV) is lower than J_1 (J_2), but still relatively large, and it supports different types of magnetic excitation like the SD phase [19]. At $M = 1.0\,\mu_B$, K is very close to J_2 and $J_1/2$. In fact, at ambient pressure and $M = 1.0\,\mu_B$, the SD phase is energetically more favorable in comparison to other magnetic phases. The range of values taken by the biquadratic term K shows relatively little changes with hydrostatic pressure (Fig. 3). For all pressures, it increases from 5 to 10 meV for the LS state to 30–35 meV in the HS state. According to the three-orbital Hubbard model [50,51], a large value of K indicates a large value of the hopping parameter between unoccupied and occupied orbitals on neighboring magnetic ions. Its dependence on the ratio of the hopping parameters rather than their absolute values may explain the relatively little variation in K as a function of pressure. As a consequence of the little variation with pressure, while at ambient pressure K is remarkably different from $J_1/2$, J_2—being larger in the intermediate magnetization and almost half in the HS state—at higher pressures takes values in a similar range, as can be seen from Table IV. The relative strength of the NNN and NN exchange couplings J_2/J_1 and of the biquadratic and NN exchange couplings K/J_1 can help interpret the phase diagram. J_2/J_1 is a measure for the competition between the CAFM and SAFM phases. A high K/J_1 value means that the simple Heisenberg model with only bilinear terms (J_1, J_2) is insufficient to describe all magnetically ordered states, and other AFM phases, such as the SD or the spin trimers, are important and indicate the presence of higher-order magnetic fluctuations like SD or spin trimers into the system.

Figure 4(a) presents the dependence of the relative strength of exchange coupling J_2/J_1 on pressure and magnetization for $M \geqslant 1.0\,\mu_B$. In the classical 2D mean-field phase diagram, the magnetic interactions $J_2/J_1 \approx 0.5$ correspond to the boundary between the SAFM/CAFM phases [52]. Within this framework, the results suggest that a SAFM/CAFM transition may be possible at ambient pressure and less likely at higher pressures. On the other hand, from a single-particle thermal occupancy viewpoint, the region of lower magnetization is harder to reach at ambient pressure because the depth of

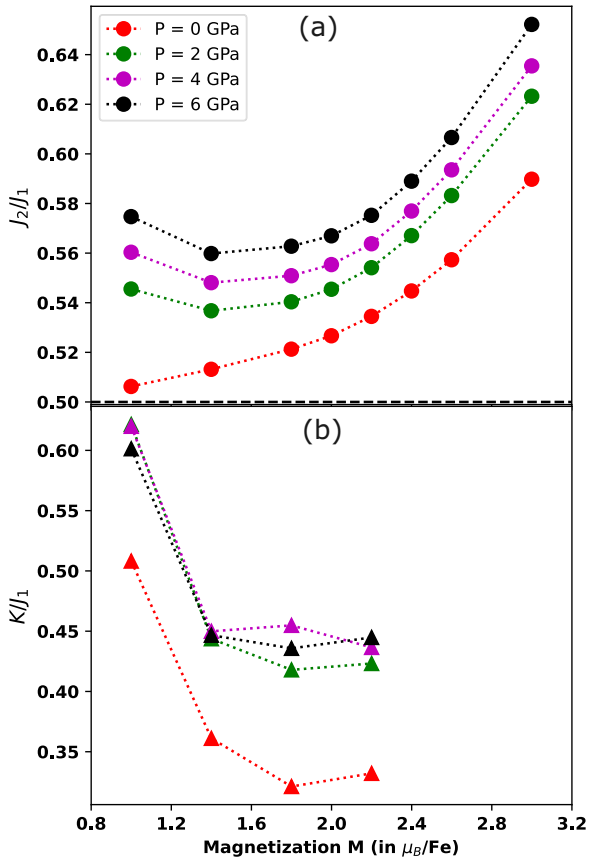

FIG. 4. Dependence on magnetization M of the ratio, (a) J_2/J_1, between the NNN and NN spin-exchange parameters, and (b) K/J_1, between the biquadratic and NN spin-exchange parameters in Eq. (1) for different values of the applied hydrostatic pressure P. $P = 0$ GPa corresponds to ambient pressure.

the energy well associated with the AFM phase at ambient pressure is roughly twice that of the value observed at higher pressure (Fig. 2). Moreover, as the pressure increases, the position of the minimum (in Table III) is moving towards smaller magnetization.

Figure 4(b) presents the dependence of K/J_1 on magnetic moment and pressure. At ambient pressure, a high value of K/J_1 ($\approx$0.31) in a high spin state means that there is room for higher-order magnetic fluctuations [19]. At higher pressure, K/J_1 further increases. Considering the concurrent reduction of the energy difference between magnetic phases, this indicates that magnetic fluctuations are increasingly likely and strong. As a consequence, the mean-field theory approach is insufficient and one has to turn to methods that account for collective phenomena. In Sec. V we build on the DFT results of this and the previous section using a field-theory approach to capture the effect of fluctuations.

C. Orbital-resolved density of states

Figure 5 presents the orbital-resolved (spin-)DOS of the t_{2g} $3d$ orbitals for the FM and CAFM and SAFM phases for different applied hydrostatic pressure. These orbitals are those that contribute the most at the Fermi surface (see Fig. 12). In the FM phase, the orbital-resolved spin-DOS is calculated at 0.2 μ_B for which FM is predicted as the most stable phase

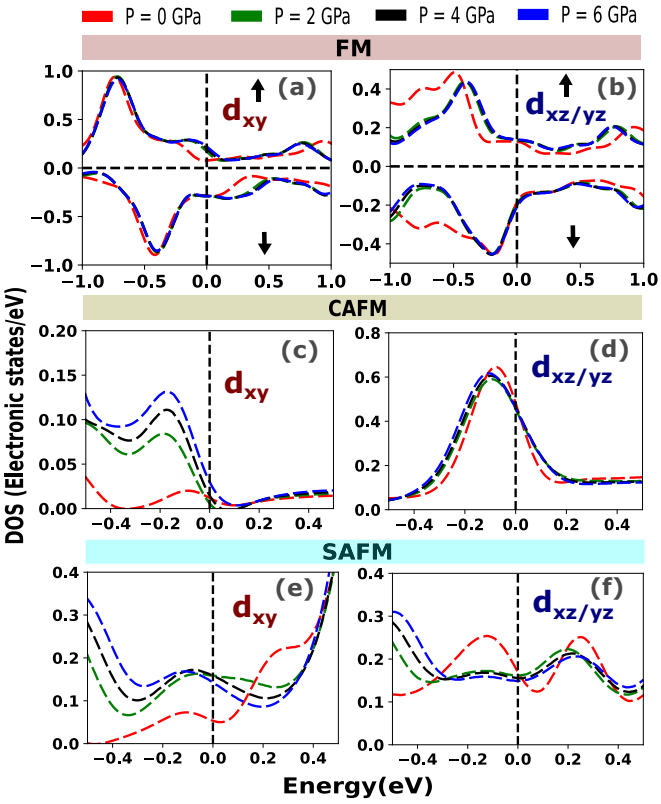

FIG. 5. Orbital-resolved spin density of states (DOS) of d_{xy} and $d_{xz/yz}$ in different magnetic phases. FM (a), (b); CAFM (c), (d); SAFM (e), (f); respectively, with pressure.

(Fig. 2)—that is, in an LS state. For the CAFM and SAFM phases, the orbital-resolved DOS is calculated at the phase optimal magnetization reported in Table III—that is, in an HS state.

At ambient pressure, the d_{xy} down-spin channel contributes dominantly to the occupied states near the Fermi level of the FM phase [Fig. 5(a)]. As pressure is increased, there is an increase in partial DOS in the up-spin channel. The difference between up- and down-spin DOS around the Fermi level decreases at higher pressure. This shift in the peak for the up-spin channel at increased pressure corresponds to a reduction in the spin-exchange parameters (see Fig. 3). At a low spin state there is a small but gradual reduction in j_1 which moves towards zero from a negative value. This indicates reduced FM fluctuations with increased pressure. For the $d_{xz/yz}$ [Fig. 5(b)], the up/down channel contribution is similar at the Fermi level and there are no substantial changes when pressure is increased.

Figure 5(d) shows that there is a significant contribution from only the $d_{xz/yz}$ orbital in the partial DOS at the Fermi level in the CAFM phase at ambient pressure. The partial DOS of the d_{xy} orbital at the Fermi level is negligible [Fig. 5(c)]. Increasing the pressure does not change the contribution at the Fermi level substantially. With pressure, the peak below the Fermi level of $d_{xz/yz}$ is slightly reduced in intensity and shifted in position to lower energies, and the smaller peak below the Fermi level for d_{xy} increases.

At ambient pressure, in the SAFM phase, both the t_{2g} and e_g orbitals contribute to the DOS at the Fermi level [Fig. 12(c)].

The $d_{xz/yz}$ has the highest contribution, whereas the d_{xy} has the lowest. Increasing pressure, the contribution d_{xy} becomes roughly equal to that of $d_{xz/yz}$ while the contribution from e_g orbitals is suppressed [Fig. 12(c)].

The overall picture that emerges from the evolution of the partial DOS with pressure is the exclusivity of the $d_{xz/yz}$ orbitals in the CAFM phase, and conversely the key role played by the d_{xy} orbital in the FM and SAFM. In particular, the enhanced d_{xy} partial DOS with pressure correlates with the reduction of FM fluctuations in the LS phase and the emergence of long-range SAFM order in the HS state.

V. 2D EFFECTIVE FIELD-THEORY MODEL

In this section, starting from the DFT results obtained and their discrepancies with experiments, we construct an effective theory for relevant collective degrees of freedom. By studying the instabilities of such field theory, we aim to understand the phase diagram of FeSe.

Experimentally, long-range spin order is observed between 2 and 6 GPa. While the DFT calculations correctly predict the disappearance of long-range magnetic order around 6 GPa, they showed a propensity towards the formation of SAFM order below 2 GPa in contrast with the experimental findings [23]. In particular, DFT results indicate that (i) the bandwidth of the d_{xy}, d_{xz}, d_{yz} orbitals is the closest to the experiment when long-range magnetic order is considered, and (ii) the values of spin-exchange parameters $J_{1,2}$ are larger while K/J is smaller at zero than at finite applied pressure. In what follows, we put forward a classical 2D spin model to reconcile the DFT results with the experimental findings.

Using a 2D model is justified by FeSe being a layered material, with a strong anisotropy of the spin-exchange parameters J, which is reflected in the spin anisotropy (see Figs. 3 and 10 in Appendix C). The classical treatment of the spin degrees of freedom is justified because, due to its multiorbital nature, FeSe is neither fully itinerant nor fully spin-localized. Then, a fraction of spin is localized, but spins can gradually change their amplitude and orientation due to free flow back and forth into the itinerant bath, which can be described classically [53]. From the results of the previous section, one may infer that at ambient pressure, the system is closer to the quantum critical point between the CAFM and SAFM phases since $J_2/J_1 \to 0.5$ (but only for LS). However, this is not the case because according to the Mermin-Wagner theorem due to fluctuations there is no long-range magnetic order (and thus no critical point) in a 2D classical system with J_1, J_2 interactions. The magnetic long-range order is frustrated even extending the 2D mean-field picture to 3D [54] and including quantum corrections in the HS state. Decisively, from the results in Ref. [55], one can deduce that the J_2/J_1 ratio we obtained at *optimal* (HS) magnetization, at a temperature $\sim$100 K, corresponds to a thermal—thus classical rather than quantum—critical regime. Then, the classical treatment of the system in the model is justified.

A. Hamiltonian for the orbital degrees of freedom

The DFT calculations show a strong dependence of the spin-exchange parameters on the local on-site magnetization, which points to a strong coupling between the spin and orbital degrees of freedom: varying the on-site magnetization is equivalent to selecting the spin configurations (high-spin or low-spin) of the Fe d-orbitals. To model the high-spin or low-spin dependence into the effective low-energy theory, we introduce a Hamiltonian for the d orbital degrees of freedom. We take fermionic annihilation operators $c_{\sigma\xi}(i)$ at a site i with spin σ and orbital ξ indexes, and we notice that the fluctuation of orbital content by analogy with spin space operators will correspond to a bosonic operator defined as $b_i = c^\dagger_{\sigma\xi}(i)c_{-\sigma\xi\pm1}(i)$. We take fermionic annihilation operators $c_{\sigma\xi}(i)$ at a site i with spin σ and orbital ξ indexes, and we notice that the fluctuation of orbital content by analogy with spin space operators, namely $S = c^\dagger_{\sigma\xi}(i)c_{-\sigma\xi}(i)$, will correspond to a bosonic operator defined as $b_i = c^\dagger_{\sigma\xi}(i)c_{\sigma\xi\pm1}(i)$ (see Appendix F). From Fig. 2, we observe that the energy difference between the lowest magnetic and the nonmagnetic configuration can be fitted as a cosine of the spin-magnetization $|S|$, $-W_L\cos(\delta|S|)$ with $\delta|S| = |S| - |S|_0$ (see Appendix C). Remarkably, W_L strongly depends on pressure, with W_L at ambient pressure being approximately twice the W_L at 2 GPa.

We then consider a basis of on-site localized bosonic states associated with the d-orbital fluctuations, and we define the following Hamiltonian in terms of creation and annihilation operators $b_i, b_i^\dagger$:

$$H_{\text{orb}} = -W_L \sum_i (b_i^\dagger b_{i+1} + \text{H.c.}) + J_H \sum_i b_i^\dagger b_i b_i^\dagger b_i, \quad (3)$$

with a next-neighbor hoppinglike term [56] W_L and a quadratic J_H Hund's exchange term [13]. In this simple tight-biding model, the hopping parameter is exactly the high-spin/low-spin energy difference that can be fitted from the curves in Fig. 2. The cosine fit works well (Fig. 10), so we can restrict ourselves to the nearest-neighbor tight-binding approximation, although in principle field theory does not require it.

Instead of working with bosons, $b^\dagger$, we further simplify the problem and work with $O(2)$ rotors: we define the angle θ as the ratio of occupancies of the d_{xy} orbital with respect to the d_{xz} and d_{yz} orbitals. Since orbital fluctuations are confined to the 2D plane and can be assumed as continuous, classical variables, we follow Villain [57] to rewrite the Hamiltonian in terms of bosonic angular fields:

$$H_{\text{orb}} = \iint dx\, dy (W_L(\nabla\theta_L)^2 + J_H(\nabla\phi_L)^2 + y_L\cos\phi_L), \quad (4)$$

where $\theta_L(x, y)$ is the orbital field, related to the local density of b-bosons, $\nabla_x\theta_L \propto b^\dagger(x)b(x)$, $\phi_L(x, y)$ is the canonically conjugated field, and y_L is the fugacity. The fugacity parameter,

$$y_L = \exp(-\epsilon\beta W_L), \quad (5)$$

is related to the temperature $T = 1/\beta$ and the low-spin/high-spin energy difference W_L [58]. The factor ϵ is the analog of the relative permittivity in 2D electric gas. The key difference with the usual Villain Hamiltonian is that due to the presence of strong correlations, the fluctuations of canonically conjugated ϕ_L field appear, which modifies the value of ϵ [59]. Namely, in the original Kosterlitz and Thouless picture $\epsilon = \pi^2/2$, including vortex screening [60] gives $\epsilon = 3/\pi$, while including the canonically conjugated term, one that is

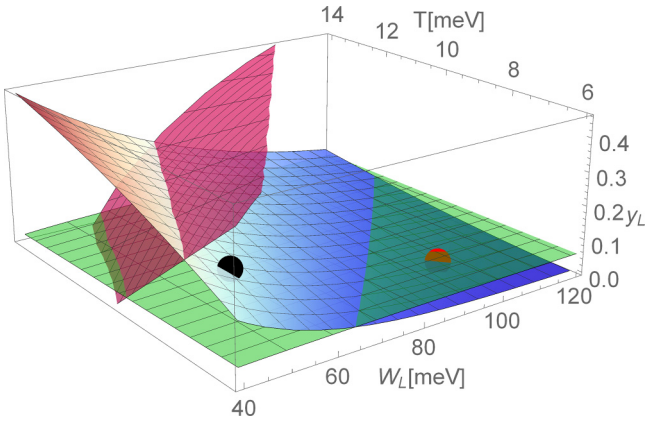

FIG. 6. Shaded blue-to-red surface shows, for $J_H = 0.6$ eV, the orbital vortex fugacity y_L, Eq. (5), as a function of the orbital fluctuations' bandwidth W_L and temperature T. Green and magenta surfaces are the lower and upper limits of the vortex crystal phase, respectively. We show the location of $P = 0$ (red dot) and $P \geqslant 2$ GPa (black dot). The red dot is just below the green plane hence in the regime where bound pairs of vortices exist but become dilute in the thermodynamic limit ($x, y \to \infty$), while the black dot is well inside the vortex crystal phase where topological orbital excitations are ordered and their number is constant.

proportional to J_H, gives an extra factor $(W_L/J_H + 2)/[2(W_L/J_H + 1)]$ to ϵ. The cosine term in Eq. (4) has been introduced in the 2D context by Villain [57] to capture low-energy large-angle fluctuations. Because of the latter term, the Hamiltonian hosts vortex excitations. The vortex excitations manifest physically as regions of gradually lower spin magnetization in an overall high-spin background. Vortexes of the size ∼10 nm have been reported in experimental studies in FeSe [61].

The value of y_L [Eq. (5)] determines the system's behavior [62,63]. This is illustrated in Fig. 6 for $J_H = 0.6$ eV—which was calculated for FeSe—[13] where y_L is shown as a function of the temperature $1/\beta$ and W_L. In the region below the green plane ($y_L = 0.054$), the system is below the vortex regime and physics is dominated by density waves. Above $y_L = 0.054$, in the region between the green and the magenta surfaces, the vortex system undergoes a crystallization transition. Long-range magnetic order is then allowed in the high-spin regions between vortices. Beyond the magenta surface, vortices move freely and static long-range magnetic order is destroyed. Extracting the values of W_L from Fig. 2, we found that slightly above 100 K, FeSe is in the density wave region at $P = 0$ GPa, while at $P = 2$ GPa it is in the vortex crystal phase. At larger pressure and lower W_L, the system is in the free vortex regime.

This result from the model agrees with the experimental observation of long-range magnetic order being observed in FeSe for intermediate pressures, while absent at ambient pressure and above 6 GPa [23]. Further, the above model provides a rationale for the tendency in the DFT results to long-range magnetic order at ambient pressure, which is not observed experimentally. The long-range magnetic order is suppressed by the orbital vortex formation because of the coupling of the spin with "randomness" present in the orbital degrees of freedom. Figure 6 shows that this randomness is present at ambient pressure, while at higher pressure the orbital sector is inside the vortex phase and becomes ordered. The suppression of the long-range spin order by vortex formation cannot be captured in standard DFT calculations on a (magnetic) unit cell, and the long-range magnetic order is favored over the nonmagnetic configuration both energetically and when considering the electronic structure close to the Fermi level. On the other hand, when DFT on large supercells is used, it has been shown [17] that random-spin configurations are energetically more favorable than the nonmagnetic ordered ones, in agreement with the model above.

B. Hamiltonian for the spin degrees of freedom

As noticed previously, the strong dependence on the spin-magnetization of the spin-exchange coefficients of the reduced Heisenberg Hamiltonian in Eq. (1) indicates a strong coupling of the spin and orbital degrees of freedom. Considering the above model for the orbital degrees of freedom [Eq. (4)], the local variations of $\nabla\phi_L$ modify the local parameters of spin fluctuations, namely on the site x_i: $\langle\nabla\phi_L(x_i)\rangle \neq 0 \Rightarrow \delta J(x_i)$ and hence the local energy of the spin system. In a mean-field picture, we have

$$J(x,y)S(x_i,y_i)S(x_{i\pm1},y_i) \approx \bar{J}\,S(x_i,y_i)S(x_{i\pm1},y_i) + \delta J(x,y)S(x_i,y_i)\langle S(x,y)\rangle \tag{6}$$

[where $\bar{J}$ is the spatial average of $J(x, y)$]. The spin-exchange parameters J result by averaging over the orbital degrees of freedom, and the variations of $\nabla\phi_L(x, y)$ (as shown in Figs. 2 and 3) result in an effective magnetic field $h(x, y) = \delta J(x, y)\langle S(x, y)\rangle$. Then, the Hamiltonian for the spin degrees of freedom coupled with the orbital degrees of freedom consists of a Heisenberg-like model, including a quadratic term [similar to Eq. (1)], and an additional term depending on $h(x, y)$:

$$H_{s(+L)} = \sum_{ij} J_{ij}\vec{S}_i \cdot \vec{S}_j - K\sum_i (\vec{S}_i \cdot \vec{S}_{i\pm1})^2 + h(x,y)[S^x(x,y) + S^y(x,y)]. \tag{7}$$

The spatial distribution of $h(x, y)$ in Eq. (7) may be either random (for the orbital density fluctuation regime at $P = 0$ GPa) or periodic (for vortex crystal, $P \geqslant 2$ GPa). In the latter case, one expects the opening of Bragg-minigaps in the spin excitation spectrum at appropriate magnetic reduced Brillouin zone boundaries. In the former case, one expects rare, randomly positioned areas of the low-spin state which will induce a variation of $J(n_L)$, hence disorder-induced localization. This is true not only when the potential associated with h changes abruptly and thus the long-range spin-order is destroyed by backscattering, but also for a sufficiently smooth potential, such that forward scattering dominates. It can be shown [64] that $h(x, y)$ introduces an exponential decay prefactor in front of any spin-spin correlation functions, and thus only a short-range spin-order is possible.

From Fig. 2, we also observe that for the lowest on-site magnetization, i.e., the largest distortion of the orbital variable, magnetic phases other than the SAFM can become

dominant, namely the FM phase. This phase can stabilize the topological excitations and also lead to local time-reversal symmetry breaking. In fact, time-reversal symmetry breaking has been detected experimentally in FeSe [65,66], and topological objects that do locally break time-reversal symmetry have been recently observed experimentally [67].

A more advanced and quantitative treatment of spin and orbital fluctuations based on the full solution of the renormalization-group equation is postponed to further study.

C. Renormalization of the electronic structure

The orbital fluctuations from Eq. (4) couple with the electronic degrees of freedom and can renormalize the electronic structure (e.g., from DFT calculations) by reducing the band dispersion. The coupling, $g_{\text{el-}L}$, between a propagating electron and a boson describing local fluctuation of orbital content can be treated like any electron-boson coupling. To estimate the band renormalization, we use the results obtained for polarons in the context of the well-studied electron-phonon coupling. Thus, we follow the standard Feynman path integral prescription to compute the renormalization coefficient for the velocity [68] α_v due to polarons:

$$\alpha_v^{-1}(\omega, \bar{g}_{\text{el-}L}) = \left(1 + \frac{\bar{g}_{\text{el-}L}}{6} + 0.025\bar{g}_{\text{el-}L}^2\right)\frac{1}{1+(\omega/W_L)^2}. \tag{8}$$

In Eq. (8), the velocity renormalization in the weak-coupling limit [68] is weighted by a Lorentzian depending on ω, the energy difference with respect to the chemical potential. We added this energy-dependent factor to the original expression in Ref. [68] to take into account that bosons cannot, because of their energies, perturb all bands but they act only close to the Fermi energy [69]. The dimensionless coupling, $\bar{g}_{\text{el-}L}$, is defined as $\bar{g}_{\text{el-}L} = g_{el-L}/\sqrt{t_{\text{el}}W_L}$. We take the unknown amplitude of electron-boson coupling, $g_{\text{el-}L}$, as a *free parameter* and we use $W_L = 150$ meV for the dispersion of the orbital fluctuations [introduced in Eq. (3)] and $t_{\text{el}} = 1$ eV for the dispersion of the electronic band. The latter values are estimates of the order of magnitude for those quantities. Then, we consider the reduction of the electron velocity α_V (thus a reduction of the band curvature) as a function of $g_{\text{el-}L}$. In principle, the coupling, thus the renormalization, can be determined from first-principles following Ref. [70], though here we only aim to roughly estimate the range of renormalization.

The renormalization of the electron's velocity from Eq. (8) is plotted in Fig. 7 as a function of the coupling parameter and the distance from the chemical potential. Close to $\omega = 0$ eV, the observed velocity can be reduced by 30% for $g_{\text{el-}L} \sim 0.2$ [71]. As one moves away from the Fermi energy, the renormalization factor goes to 1—no renormalization. The strong energy dependence implies that the effect should be distinguishable from the Hubbard U mechanisms of bandwidth renormalization and that care needs to be taken if one attempts to infer the bandwidth from a partial dispersion relation.

We expect the renormalization to be larger for the band with d_{xy} character because of concurrent effects. First, this band has the smallest DFT dispersion, and the dispersion enters into the denominator of the dimensionless coupling

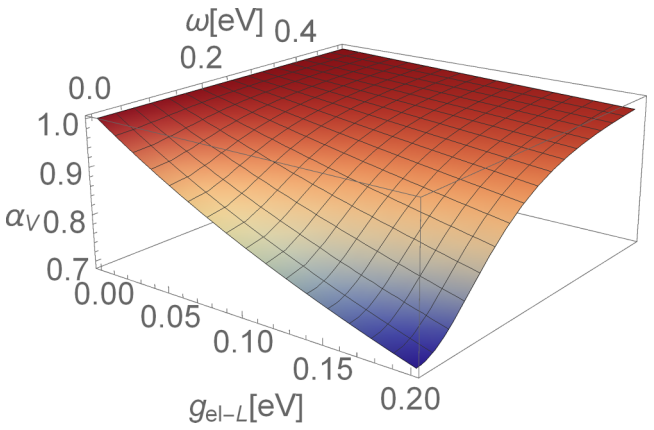

FIG. 7. Renormalization factor α_v of an electron's velocity, from Eq. (8), as a function of coupling between single carriers and orbital fluctuations $g_{\text{el-}L}$ and distance from the chemical potential ω.

$\propto g_{\text{el-}L}$. Second, by construction, the orbital field θ_L in Eq. (4) is zero at high spin and maximum at the low spin state when the occupancy of the d_{xy} orbital changes from 1 to 0 (while the occupancy of the degenerate $d_{xz,yz}$ changes by a fraction between 1 and 2). Then, d_{xy} is most affected by orbital fluctuation, and as such we expect a larger reduction in the bandwidth than for $d_{xz,yz}$. This is consistent with what was observed in ARPES experiments.

For the above-given renormalization effect, we only considered the first two terms in Eq. (4), i.e., orbital occupancy density waves. In principle, also electrons couple to the vortices described by the last term in Eq. (4). The reason we did not consider this last term is that a theory for such coupling is not available, although one can anticipate that the coupling is the largest for electron dispersion close to the Γ point (due to the k-dependence of the Fourier-transform of a solitonic wave) and that there are several satellites separated by ∼0.1 eV [72], which may be visible in experimental spectra.

VI. CONCLUSIONS

Using DFT at the generalized gradient approximation level, we calculated the dependence of the magnetic formation energy of FeSe on the local magnetization for different magnetic phases, and we mapped the results into a Heisenberg-like Hamiltonian with two main outcomes. First, we observed a strong dependence of the spin-exchange parameters extracted from the Heisenberg-like Hamiltonian on the local on-site magnetization, which points to a *strong coupling between spin and orbital degrees of freedom*. Second, we obtained stable antiferromagnetic orderings at ambient pressure. The latter result is consistent with the results we obtained for the electronic structure, where assuming an antiferromagnetic ordering renormalizes the bandwidth of the d-bands, bringing it closer to the ARPES results. On the other hand, this propensity towards an antiferromagnetic phase is in disagreement with experimental results where magnetic ordering is observed only for a pressure of 2 GPa or larger.

We argued that though a thermodynamically stable long-range magnetic order at ambient pressure has not been detected, the DFT results, together with classical field theory

arguments, may indicate the existence of a short magnetic order convoluted with slow variations of spin amplitude at long range. Such an inhomogeneous spin pattern would emerge from the strong coupling between the spin and orbital fluctuations and from the quasi-2D nature of FeSe. Indeed, we showed that the DFT results can be reconciled with the experimental observations within a *2D effective field theory, which admits nontrivial, spatially extended topological vortex states*. According to the model, the formation of vortices both suppresses the antiferromagnetic phase at ambient pressure and plays a role in renormalizing the bandwidth of d-band. The existence of mesoscopic structure such as vortices is comforted by the recent observation of Griffiths phases [31] in $FeSe_{1-x}S_x$.

This 2D effective field-theory model implies the impossibility of capturing the bandwidth renormalization of FeSe close to the Fermi energy uniquely by improving the description of electron correlation beyond DFT, and instead points to the need to account for spin and orbital fluctuations at the mesoscopic scale. Our DFT results for the electronic structure hint that to partly reproduce such an effect—without resorting to large supercells as in Ref. [17]—a "poor man's" approach would be to assume an antiferromagnetic ordering. A more sound approach is to account for the interaction between electrons and the fluctuations via a polaronic-like model. Our preliminary results show that the electronic structure obtained with DFT can indeed be renormalized up to 30%, and the most affected band would be that with d_{xy} character.

Finally, the 2D effective field-theory model presented here—or rather a refined version of it based on the full solution of the renormalization-group equation—together with the results on the existence of an SD magnetic ordering—which we found to be energetically favored for intermediate magnetization—can be used to investigate the origin of the nematic phase in FeSe.

The data that support the findings of this article are openly available at repository for research data MaterialsCloud [80].

ACKNOWLEDGMENTS

This work was supported by the Engineering and Physical Sciences Research Council (EPSRC), under Grant No. EP/V029908/1. The authors are grateful for the use of the computing facilities and support from the Northern Ireland High Performance Computing (NI-HPC) service funded by EPSRC (EP/T022175/1) and the UK national high-performance computing service, ARCHER2, through the UKCP consortium funded by EPSRC (EP/X035891/1). P.C. acknowledges financial support of the National Science Centre (NCN - Poland) through Grant No. 2021/43/B/ST8/03207. The authors acknowledge useful discussions with N. Hussey, A. Carrington, S. Acharya, and M. Gabay.

APPENDIX A: DEFINITION OF BANDWIDTH

As discussed in the main text, in this manuscript we refer to the difference between the maximum and the minimum band energy of the band dispersion along the Γ-M direction as "bandwidth." This is depicted schematically in Fig. 8.

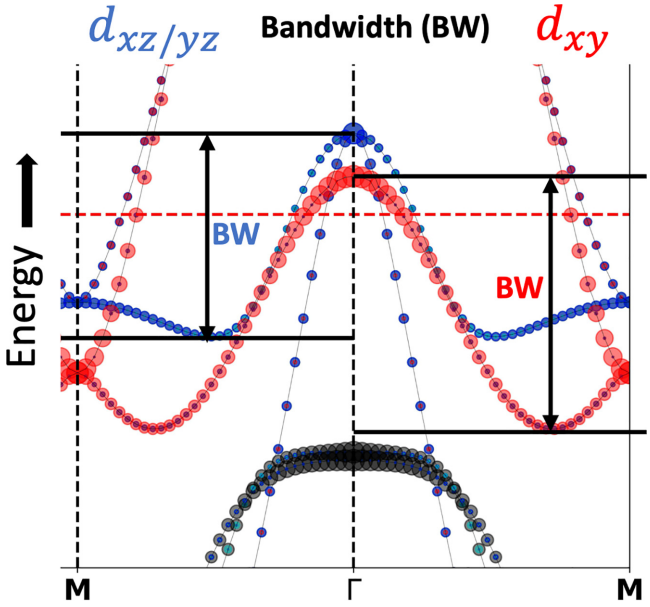

FIG. 8. Dispersion of d_{xy} (red dot) and $d_{xz/yz}$ (blue dot) in the M-Γ-M direction obtained from DFT calculations. The bandwidth (BW) is defined as the difference between the maximum and the minimum band energy.

APPENDIX B: EVOLUTION OF STRUCTURAL PARAMETERS WITH PRESSURE IN DIFFERENT MAGNETIC PHASES

The evolution of different structural parameters such as the internal z position of Se (z_{Se}), the c/a ratio, and the height of the Se-atom from the Fe-plane (h_{Se}), is presented in Fig. 9. A comparison of our DFT calculated structural parameters with experiment is presented in Table V. A linear increase in z_{Se} with pressure in nonmagnetic phase and with different long-range magnetic order is very much evident from Fig. 9(a). At ambient pressure, the calculated value in nonmagnetic phase is very close (slightly underestimated) to the experimental as well as the DFT + DMFT calculated value [73–75]. Introducing long-range order into the system slightly overestimates the value. At higher pressures (4 GPa), the experimental z_{Se} is very close to the calculated value with SAFM long-range order. Looking at the lattice parameters reveals a decreasing trend in the c/a ratio with pressure [Fig. 9(b)], which is consistent with experiments. Calculated c/a at ambient pressure is overestimated by 2% with respect to the experimental value and very close to DFT + DMFT results. The lattice parameters are kept fixed for the calculations with long-range magnetic order. Anion height (h_{Se}) has been found to be an important factor controlling magnetism as well as superconductivity in iron-based superconductors [76]. Therefore, it is worth investigating the variation of h_{Se} at different magnetic phases with external hydrostatic pressure. Figure 9(c) shows the variation of h_{Se} with pressure. The variations in NM, CAFM, and SAFM phases are presented with blue, green, and red, respectively. If we look at the NM phase, it is conspicuous that there is a gradual increase in h_{Se} with pressure. A steep increase is evident at lower pressure values, which ultimately reaches almost saturation at pressure

TABLE V. Comparison of structural parameters.

Structural parameters	DFT (NM)	DFT+CAFM	DFT+SAFM	Experiment
z_{Se} (0 GPa)	0.2550	0.2697	0.2726	0.2660
z_{Se} (4 GPa)	0.2673	0.2790	0.2823	0.2915
c/a (0 GPa)	1.4900	–	–	1.4580
c/a (4 GPa)	1.4583	–	–	1.4215
h_{Se} (Å) (0 GPa)	1.3927	1.4734	1.4891	1.4502
h_{Se} (Å) (4 GPa)	1.4107	1.4725	1.4904	1.4233

greater than 5.0 GPa. Magnetic interactions seem to increase h_{Se} to a great extent. The calculated value of h_{Se} at ambient pressure with optimized structure is 1.3927 Å in nonmagnetic phase. The value is underestimated by nearly 4% in comparison to experiments. h_{Se} is increased to 1.4734 and 1.4891 Å in CAFM and SAFM phase, respectively. The situation improves as long-range order is introduced into the system, and the value is within 2% of overestimation. The variation in CAFM phase is marked by an increase in h_{Se} at $P = 1.0$ GPa, beyond which it is decreased gradually. The rate of decrement is faster at pressure greater than 4.0 GPa. In the case of SAFM, the nature of variation is somewhat different in comparison to CAFM. A sudden increase in h_{Se} is followed by a plateau up to pressure 3.0 GPa. A gradual reduction in h_{Se} just like CAFM is observed beyond 3.0 GPa. From the above discussion, it is evident that the structural parameters calculated via our DFT approach exhibit strong agreement with experimental results, both in nonmagnetic and long-range magnetic ordered FeSe.

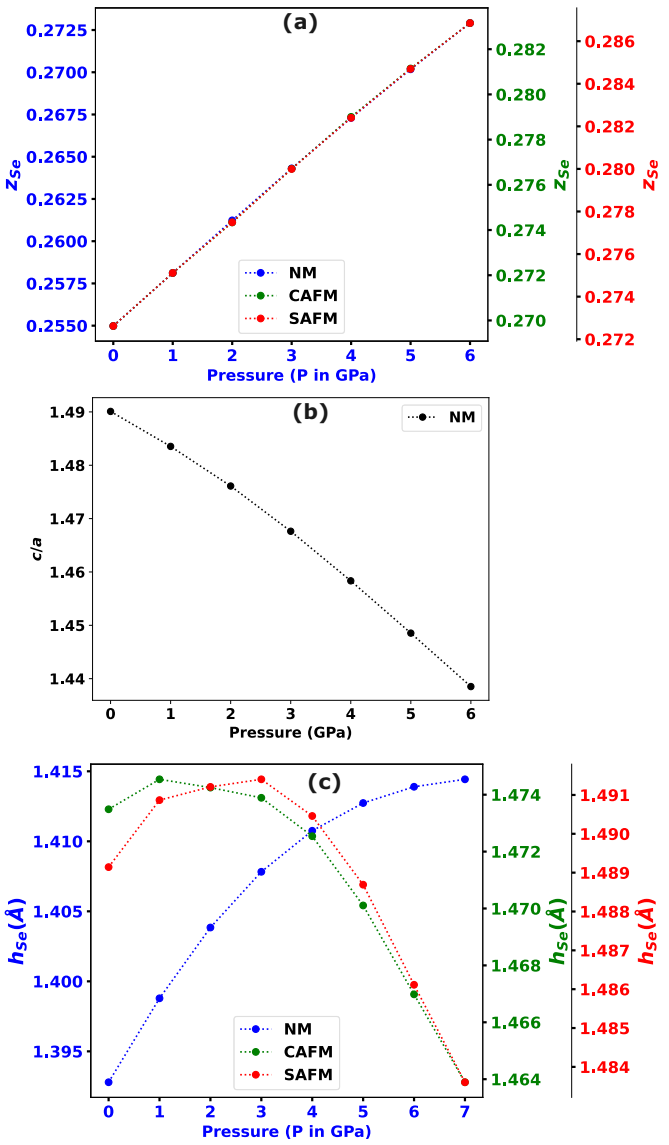

FIG. 9. Variation of (a) z_{Se}, (b) c/a, and (c) h_{Se} with pressure in nonmagnetic (NM), checkerboard/Neél antiferromagnetic (CAFM), and striped AFM (SAFM) phase.

APPENDIX C: COSINE FITS $J_{1,2}$

Interestingly, the data for the *effective* J_1, J_2 can be well-fitted (Fig. 10) with a cosine-like function of the magnetization: $w[-\cos(aM + \alpha) + c]$, where w is the "width" and c is the "offset" of the fitted curve (Table VI). The absolute value of the parameter w decreases with an increase in pressure. This denotes decreased J_{eff} with increased pressure. On the other hand, the parameter c favors AFM over FM. A gradual increase in the absolute value of c is observed with increased pressure. This indicates possible FM fluctuation at ambient pressure and higher stability of the AFM state at higher pressure in FeSe.

APPENDIX D: BIQUADRATIC K FROM NONCOLLINEAR CALCULATION

As discussed in the main text, the biquadratic exchange K is obtained by performing total-energy noncollinear calculations on magnetic unit cells obtained by rotating the angle θ between the two interpenetrating magnetic sublattices shown in Fig. 1(b). The difference $\Delta E(\theta)$ between the total energy at a given θ and the energy of the SAFM phase ($\theta = 0$)

TABLE VI. Fitting parameters.

Parameters	$P = 0$ GPa	$P = 2$ GPa	$P = 4$ GPa	$P = 6$ GPa
$w(j_1/2)$	−34.43	−26.51	−23.89	−21.57
$a(j_1/2)$	−1.15	1.14	1.15	1.16
$\alpha(j_1/2)$	15.44	3.42	3.39	3.38
$c(j_1/2)$	−0.63	−0.60	−0.63	−0.66
$w(j_2)$	−38.90	−32.41	−29.93	−27.78
$a(j_2)$	1.05	0.98	0.98	0.98
$\alpha(j_2)$	6.62	3.60	3.59	3.60
$c(j_2)$	0.60	−0.52	−0.54	−0.56

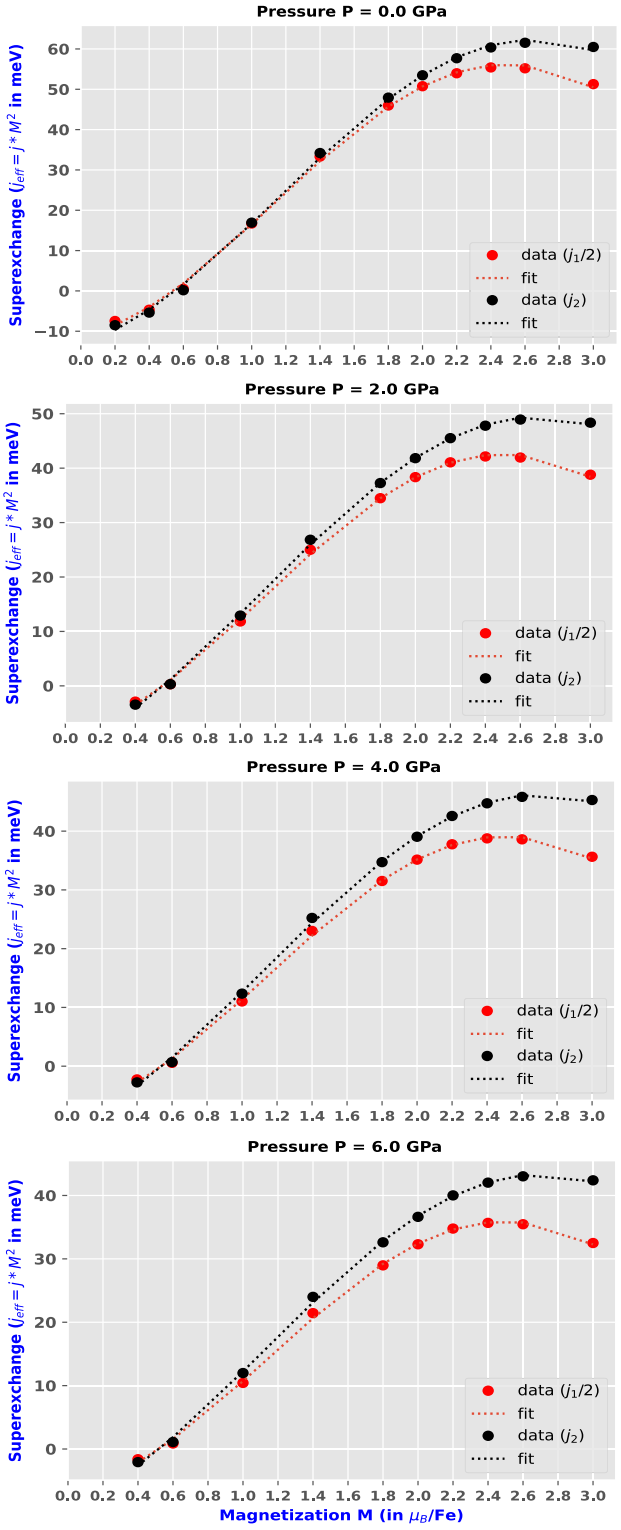

FIG. 10. $J_1/2$ (red dots) and J_2 (black dots) values as a function of the magnetization and the corresponding cosine fit (red dashed for $J1/2$ and black dashed for J_2). The coefficients of the fit are given in Table VI. See the text for details.

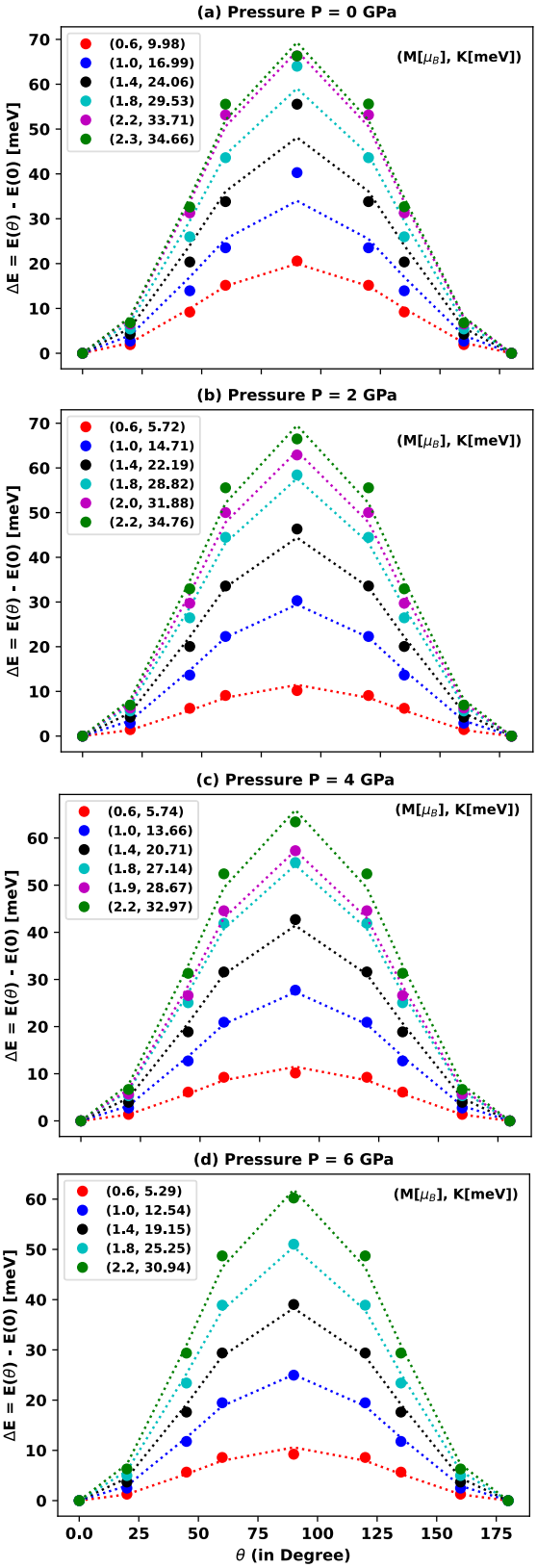

FIG. 11. The variation of total energy by changing the angle θ between the magnetic sublattices with respect to the energy in the SAFM phase ($\theta = 0$), calculated at different pressures and magnetic moments. In the legend, we report, in parentheses, the magnetic moment and the K biquadratic exchange parameter extracted by fitting the curve. See the text.

is presented in Fig. 11 at different magnetic moments and pressure. The value of K at each magnetic moment has been extracted by fitting Eq. (2) with a simple least-squares fitting

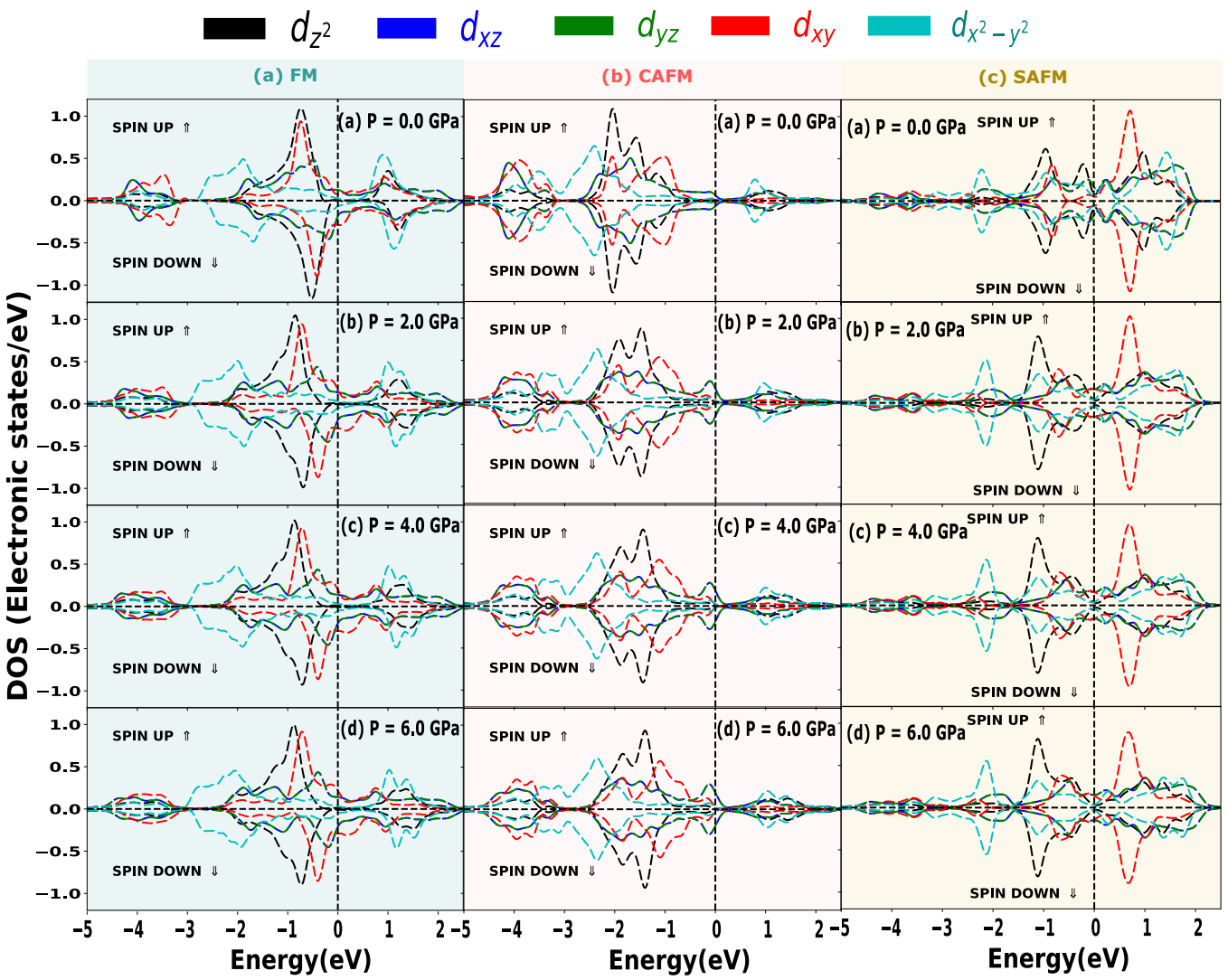

FIG. 12. Variation of spin-resolved partial DOS of all the Fe-3d orbitals with pressure in different magnetic phases.

method. From Fig. 11, one can see that a better fit is obtained for high spin states than for the low spin ones.

APPENDIX E: SPIN-RESOLVED PARTIAL DOS

Spin-resolved DOSs of t_{2g} and e_g orbitals are presented in Fig. 12. A higher partial DOS of t_{2g} in comparison to e_g around the Fermi level is conspicuous in FM and CAFM at ambient pressure. All five d-orbitals have a finite contribution near the Fermi level in the case of SAFM. Even $d_{x^2-y^2}/d_{z^2}$ have a greater contribution in comparison to d_{xy} around the Fermi level. As soon as external pressure is applied on the system, the partial DOS of the e_g states is observed to be quenched.

APPENDIX F: ORBITAL FLUCTUATIONS AS BOSONIC OPERATORS

The model Hamiltonian for the fermions can be written as

$$H_f = K + V, \tag{F1}$$

i.e., the sum of a kinetic part, K, and a potential part, V. The kinetic part maps the Kohn-Sham results in a tight-binding Hamiltonian,

$$K = \sum_{\xi} \epsilon_{\xi} \sum_{i\sigma} c^{\dagger}_{\sigma\xi}(i) c_{\sigma\xi}(i) - t_{\xi} \sum_{ij,\sigma} c^{\dagger}_{\sigma\xi}(i) c_{\sigma\xi}(j), \tag{F2}$$

where i, j indicate the unit cell, $\sigma \in \{\uparrow, \downarrow\}$ indicates the spin, and ξ indicates the band index. ϵ_{ξ} and t_{ξ} are, respectively, the on-site and hopping constants for each band ξ. $c^{\dagger}_{\sigma\xi}(i)$ and $c_{\sigma\xi}(i)$ denote the creation and annihilation operator for a fermion at unit cell i, with spin σ and band ξ.

The potential part V accounts for the electron-electron interaction, which has not been accounted for within the effective single-particle Kohn-Sham picture,

$$V = \sum_{i,j} \sum_{pqrs} V_{pq;rs}(ij) c^{\dagger}_{p}(i) c_{q}(i) c^{\dagger}_{r}(j) c_{s}(j), \tag{F3}$$

where $V_{pq;rs}$ is the matrix element of the effective interaction between fermions, usually originating from Coulomb interaction. Here, for simplicity, we use $pqrs$ as collective indexes for the band and spin. Since $V_{pq;rs} = V_{rs;pq}$, V has a quadratic form in $c^{\dagger}_{p}(i) c_{q}(i)$ and it can be transformed into the normal

form,

$$V = \sum_{\alpha} \lambda_{\alpha}(ij)\rho_{\alpha}^{2}(ij), \quad \lambda_{\alpha} \in \mathbb{R}, \tag{F4}$$

where ρ_α is given by some linear combination of $c_p^\dagger(i)c_q(i)$, i.e., we made a decoupling in a particle-hole channel.

Treating exactly the Coulomb part is extremely cumbersome and only possible for systems with few electrons. Furthermore, since part of the correlation is accounted for within the Kohn-Sham scheme, $V_{pq;rs}$ is generally unknown. Here, we determine an approximation for V by choosing ρ_ν so as to select the density fluctuations that are most relevant to describe the physics of the system. In particular, we consider here only the t_{2g} bands with orbital character $d_{xz,yz}$ corresponding to $|L_z| = 1$ and d_{xy} corresponding to $|L_z| = 2$. We introduce $\tilde{\mathbf{L}}$, an effective pseudospin operator ($|\tilde{L}| = 1/2$) with components,

$$\tilde{L}_{\mathrm{j}} = c_{\sigma\xi}^{\dagger}\hat{\nu}_{\xi\xi'}^{\mathrm{j}}c_{\sigma\xi'}, \quad \mathrm{j} = x, y, z,$$

defined though the Pauli matrices in orbital space, $\hat{\nu}^{\mathrm{j}}$ (here, we illustrated again the spin and orbital indexes). Since $\tilde{L}$ is a linear combination of $c_p^\dagger(i)c_q(i)$, $\tilde{L}(i)\cdot\tilde{L}(j)$ can be identified with $\rho_\alpha^2(ij)$. We can then apply a usual Holstein-Primakoff transformation [77], and express the pseudospin raising, $\tilde{L}^+$, and lowering, $\tilde{L}^-$, operators in terms of boson $b^\dagger$, b, respectively [in the large $|L|$ limit, the formula $\tilde{L}^+(i) \approx b^\dagger(i)$ becomes exact]. These operators define density fluctuations between $d_{xz,yz}$ and d_{xy}, and they correspond to the creation and annihilation, $b_i^\dagger$, b_i, of a boson at the site i. Thus, letting $\xi \in (1, 2)$ indicate $|L_z|$ corresponding to the orbital, the bosonic operators can be written in terms of the fermionic operators as

$$b_i = c_{\sigma\xi}^{\dagger}(i)c_{\sigma\xi\pm1}(i), \quad \xi \in \{1, 2\}.$$

Working in analogy with spin, where the Heisenberg-like Hamiltonian models the spin-dynamics, one can thus introduce a model Hamiltonian to model the dynamics of the orbital fluctuations, as we do in Eq. (3).

[1] F.-C. Hsu, J.-Y. Luo, K.-W. Yeh, T.-K. Chen, T.-W. Huang, P. M. Wu, Y.-C. Lee, Y.-L. Huang, Y.-Y. Chu, D.-C. Yan, and M.-K. Wu, Superconductivity in the PbO-type structure α-FeSe, Proc. Natl. Acad. Sci. USA **105**, 14262 (2008).

[2] T. M. McQueen, A. J. Williams, P. W. Stephens, J. Tao, Y. Zhu, V. Ksenofontov, F. Casper, C. Felser, and R. J. Cava, Tetragonal-to-orthorhombic structural phase transition at 90 k in the superconductor $Fe_{1.01}Se$, Phys. Rev. Lett. **103**, 057002 (2009).

[3] R. M. Fernandes, A. V. Chubukov, and J. Schmalian, What drives nematic order in iron-based superconductors? Nat. Phys. **10**, 97 (2014).

[4] J.-F. Ge, Z.-L. Liu, C. Liu, C.-L. Gao, D. Qian, Q.-K. Xue, Y. Liu, and J.-F. Jia, Superconductivity above 100 k in single-layer FeSe films on doped $SrTiO_3$, Nat. Mater. **14**, 285 (2015).

[5] P. O. Sprau, A. Kostin, A. Kreisel, A. E. Böhmer, V. Taufour, P. C. Canfield, S. Mukherjee, P. J. Hirschfeld, B. M. Andersen, and J. C. S. Davis, Discovery of orbital-selective cooper pairing in FeSe, Science **357**, 75 (2017).

[6] P. Massat, D. Farina, I. Paul, S. Karlsson, P. Strobel, P. Toulemonde, M.-A. Méasson, M. Cazayous, A. Sacuto, S. Kasahara, T. Shibauchi, Y. Matsuda, and Y. Gallais, Charge-induced nematicity in FeSe, Proc. Natl. Acad. Sci. USA **113**, 9177 (2016).

[7] M. Yi, Y. Zhang, Z.-X. Shen, and D. Lu, Role of the orbital degree of freedom in iron-based superconductors, npj Quantum Mater. **2**, 57 (2017).

[8] M. D. Watson, T. K. Kim, A. A. Haghighirad, N. R. Davies, A. McCollam, A. Narayanan, S. F. Blake, Y. L. Chen, S. Ghannadzadeh, A. J. Schofield, M. Hoesch, C. Meingast, T. Wolf, and A. I. Coldea, Emergence of the nematic electronic state in FeSe, Phys. Rev. B **91**, 155106 (2015).

[9] M. Yi, H. Pfau, Y. Zhang, Y. He, H. Wu, T. Chen, Z. R. Ye, M. Hashimoto, R. Yu, Q. Si, D.-H. Lee, P. Dai, Z.-X. Shen, D. H. Lu, and R. J. Birgeneau, Nematic energy scale and the missing electron pocket in FeSe, Phys. Rev. X **9**, 041049 (2019).

[10] T. Yamada and T. Tohyama, Multipolar nematic state of nonmagnetic FeSe based on DFT + u, Phys. Rev. B **104**, L161110 (2021).

[11] H. Lohani, P. Mishra, and B. Sekhar, Investigation of correlation effects in FeSe and FeTe by LDA + U method, Physica C **512**, 54 (2015).

[12] S. Mandal, P. Zhang, S. Ismail-Beigi, and K. Haule, How correlated is the $FeSe/SrTiO_3$ system? Phys. Rev. Lett. **119**, 067004 (2017).

[13] S. Acharya, D. Pashov, F. Jamet, and M. van Schilfgaarde, Electronic origin of T_c in bulk and monolayer FeSe, Symmetry **13**, 169 (2021).

[14] X. Long, S. Zhang, F. Wang, and Z. Liu, A first-principle perspective on electronic nematicity in FeSe, npj Quantum Mater. **5**, 50 (2020).

[15] P. V. Arribi and L. de' Medici, Hund-enhanced electronic compressibility in FeSe and its correlation with T_c, Phys. Rev. Lett. **121**, 197001 (2018).

[16] T. Gorni, P. V. Arribi, M. Casula, and L. de' Medici, Accurate modeling of FeSe with screened fock exchange and hund metal correlations, Phys. Rev. B **104**, 014507 (2021).

[17] Z. Wang, X.-G. Zhao, R. Koch, S. J. L. Billinge, and A. Zunger, Understanding electronic peculiarities in tetragonal FeSe as local structural symmetry breaking, Phys. Rev. B **102**, 235121 (2020).

[18] The paramagnetic supercell was introduced in Ref. [78]. It is a finite supercell realization of a polymorphous paramagnet obtained using the special quasirandom structure construct [79].

[19] J. K. Glasbrenner, I. I. Mazin, H. O. Jeschke, P. J. Hirschfeld, R. M. Fernandes, and R. Valentí, Effect of magnetic frustration on nematicity and superconductivity in iron chalcogenides, Nat. Phys. **11**, 953 (2015).

[20] Q. Wang, Y. Shen, B. Pan, X. Zhang, K. Ikeuchi, K. Iida, A. D. Christianson, H. C. Walker, D. T. Adroja, M. Abdel-Hafiez, X. Chen, D. A. Chareev, A. N. Vasiliev, and J. Zhao, Magnetic ground state of FeSe, Nat. Commun. **7**, 12182 (2016).

[21] J. Pelliciari, S. Karakuzu, Q. Song, R. Arpaia, A. Nag, M. Rossi, J. Li, T. Yu, X. Chen, R. Peng, M. García-Fernández, A. C. Walters, Q. Wang, J. Zhao, G. Ghiringhelli, D. Feng, T. A. Maier, K.-J. Zhou, S. Johnston, and R. Comin, Evolution of spin excitations from bulk to monolayer FeSe, Nat. Commun. **12**, 3122 (2021).

[22] R. M. Fernandes, A. I. Coldea, H. Ding, I. R. Fisher, P. J. Hirschfeld, and G. Kotliar, Iron pnictides and chalcogenides: A new paradigm for superconductivity, Nature (London) **601**, 35 (2022).

[23] J. P. Sun, K. Matsuura, G. Z. Ye, Y. Mizukami, M. Shimozawa, K. Matsubayashi, M. Yamashita, T. Watashige, S. Kasahara, Y. Matsuda, J.-Q. Yan, B. C. Sales, Y. Uwatoko, J.-G. Cheng, and T. Shibauchi, Dome-shaped magnetic order competing with high-temperature superconductivity at high pressures in FeSe, Nat. Commun. **7**, 12146 (2016).

[24] K. Matsuura, Y. Mizukami, Y. Arai, Y. Sugimura, N. Maejima, A. Machida, T. Watanuki, T. Fukuda, T. Yajima, Z. Hiroi, K. Y. Yip, Y. C. Chan, Q. Niu, S. Hosoi, K. Ishida, K. Mukasa, S. Kasahara, J. G. Cheng, S. K. Goh, Y. Matsuda *et al.*, Maximizing T_c by tuning nematicity and magnetism in $FeSe_{1-x}S_x$ superconductors, Nat. Commun. **8**, 1143 (2017).

[25] J. Li, B. Lei, D. Zhao, L. P. Nie, D. W. Song, L. X. Zheng, S. J. Li, B. L. Kang, X. G. Luo, T. Wu, and X. H. Chen, Spin-orbital-intertwined nematic state in FeSe, Phys. Rev. X **10**, 011034 (2020).

[26] H. Pfau, M. Yi, M. Hashimoto, T. Chen, P.-C. Dai, Z.-X. Shen, S.-K. Mo, and D. Lu, Quasiparticle coherence in the nematic state of FeSe, Phys. Rev. B **104**, L241101 (2021).

[27] S.-H. Baek, D. V. Efremov, J. M. Ok, J. S. Kim, J. van den Brink, and B. Büchner, Orbital-driven nematicity in FeSe, Nat. Mater. **14**, 210 (2015).

[28] J. K. Glasbrenner, J. P. Velev, and I. I. Mazin, First-principles study of the minimal model of magnetic interactions in Fe-based superconductors, Phys. Rev. B **89**, 064509 (2014).

[29] A. Baum, H. N. Ruiz, N. Lazarević, Y. Wang, T. Böhm, R. H. Ahangharnejhad, P. Adelmann, T. Wolf, Z. V. Popović, B. Moritz, T. P. Devereaux, and R. Hackl, Frustrated spin order and stripe fluctuations in FeSe, Commun. Phys. **2**, 14 (2019).

[30] Y. Gu, Q. Wang, H. Wo, Z. He, H. C. Walker, J. T. Park, M. Enderle, A. D. Christianson, W. Wang, and J. Zhao, Frustrated magnetic interactions in FeSe, Phys. Rev. B **106**, L060504 (2022).

[31] P. Reiss, D. Graf, A. A. Haghighirad, T. Vojta, and A. I. Coldea, Signatures of a quantum griffiths phase close to an electronic nematic quantum phase transition, Phys. Rev. Lett. **127**, 246402 (2021).

[32] P. Giannozzi, S. Baroni, N. Bonini, M. Calandra, R. Car, C. Cavazzoni, D. Ceresoli, G. L. Chiarotti, M. Cococcioni, I. Dabo, A. D. Corso, S. de Gironcoli, S. Fabris, G. Fratesi, R. Gebauer, U. Gerstmann, C. Gougoussis, A. Kokalj, M. Lazzeri, L. Martin-Samos *et al.*, QUANTUM ESPRESSO: A modular and open-source software project for quantum simulations of materials, J. Phys.: Condens. Matter **21**, 395502 (2009).

[33] P. Giannozzi, O. Andreussi, T. Brumme, O. Bunau, M. B. Nardelli, M. Calandra, R. Car, C. Cavazzoni, D. Ceresoli, M. Cococcioni, N. Colonna, I. Carnimeo, A. D. Corso, S. de Gironcoli, P. Delugas, R. A. DiStasio, A. Ferretti, A. Floris, G. Fratesi, G. Fugallo *et al.*, Advanced capabilities for materials modelling with QUANTUM ESPRESSO, J. Phys.: Condens. Matter **29**, 465901 (2017).

[34] A. D. Corso, Pseudopotentials periodic table: From H to Pu, Comput. Mater. Sci. **95**, 337 (2014).

[35] J. P. Perdew, K. Burke, and M. Ernzerhof, Generalized gradient approximation made simple, Phys. Rev. Lett. **77**, 3865 (1996).

[36] J. P. Perdew, K. Burke, and M. Ernzerhof, Generalized gradient approximation made simple [Phys. Rev. Lett. **77**, 3865 (1996)], Phys. Rev. Lett. **78**, 1396 (1997).

[37] M. Cococcioni and S. de Gironcoli, Linear response approach to the calculation of the effective interaction parameters in the LDA + U method, Phys. Rev. B **71**, 035105 (2005).

[38] S. Baroni, P. Giannozzi, and A. Testa, Green's-function approach to linear response in solids, Phys. Rev. Lett. **58**, 1861 (1987).

[39] M. Aichhorn, S. Biermann, T. Miyake, A. Georges, and M. Imada, Theoretical evidence for strong correlations and incoherent metallic state in FeSe, Phys. Rev. B **82**, 064504 (2010).

[40] M. D. Watson, S. Backes, A. A. Haghighirad, M. Hoesch, T. K. Kim, A. I. Coldea, and R. Valentí, Formation of hubbard-like bands as a fingerprint of strong electron-electron interactions in FeSe, Phys. Rev. B **95**, 081106(R) (2017).

[41] H. J. Monkhorst and J. D. Pack, Special points for Brillouin-zone integrations, Phys. Rev. B **13**, 5188 (1976).

[42] M. Iraola, J. L. Mañes, B. Bradlyn, M. K. Horton, T. Neupert, M. G. Vergniory, and S. S. Tsirkin, Irrep: Symmetry eigenvalues and irreducible representations of *ab initio* band structures, Comput. Phys. Commun. **272**, 108226 (2022).

[43] P. V. C. Medeiros, S. Stafström, and J. Björk, Effects of extrinsic and intrinsic perturbations on the electronic structure of graphene: Retaining an effective primitive cell band structure by band unfolding, Phys. Rev. B **89**, 041407(R) (2014).

[44] P. V. C. Medeiros, S. S. Tsirkin, S. Stafström, and J. Björk, Unfolding spinor wave functions and expectation values of general operators: Introducing the unfolding-density operator, Phys. Rev. B **91**, 041116(R) (2015).

[45] S. R. Billeter, A. J. Turner, and W. Thiel, Linear scaling geometry optimisation and transition state search in hybrid delocalised internal coordinates, Phys. Chem. Chem. Phys. **2**, 2177 (2000).

[46] K. Liu, Z.-Y. Lu, and T. Xiang, Nematic antiferromagnetic states in bulk FeSe, Phys. Rev. B **93**, 205154 (2016).

[47] K. Momma and F. Izumi, *VESTA3* for three-dimensional visualization of crystal, volumetric and morphology data, J. Appl. Crystallogr. **44**, 1272 (2011).

[48] S. Pokharel and H. Fu, Understanding the importance of local magnetic moment in monolayer FeSe, Phys. Rev. B **104**, 195110 (2021).

[49] We consider the *effective* values for the NN and NNN parameters, $J_i \times M^2$, $i = 1, 2$.

[50] F. Mila and F.-C. Zhang, On the origin of biquadratic exchange in spin 1 chains, Eur. Phys. J. B **16**, 7 (2000).

[51] J. Y. Ni, X. Y. Li, D. Amoroso, X. He, J. S. Feng, E. J. Kan, S. Picozzi, and H. J. Xiang, Giant biquadratic exchange in 2D magnets and its role in stabilizing ferromagnetism of $NiCl_2$ monolayers, Phys. Rev. Lett. **127**, 247204 (2021).

[52] T. Yildirim, Origin of the 150-k anomaly in lafeaso: Competing antiferromagnetic interactions, frustration, and a structural phase transition, Phys. Rev. Lett. **101**, 057010 (2008).

[53] K. Temme, M. M. Wolf, and F. Verstraete, Stochastic exclusion processes versus coherent transport, New J. Phys. **14**, 075004 (2012).

[54] T. Yildirim, A. B. Harris, and E. F. Shender, Three-dimensional ordering in bct antiferromagnets due to quantum disorder, Phys. Rev. B **53**, 6455 (1996).

[55] I. Frérot and T. Roscilde, Reconstructing the quantum critical fan of strongly correlated systems using quantum correlations, Nat. Commun. **10**, 577 (2019).

[56] Strictly speaking, the cosine dependence $-W_L \cos(\delta|S|)$ defines an analog of a ξ-distortion potential, and then following analogy with elasticity, we define "elastic" modes of fluctuation in orbital space, and we take that the origin of these fluctuations is the locally modified tight-binding parameter $\delta t \sim \delta|S|$.

[57] J. Villain, Theory of one- and two-dimensional magnets with an easy magnetization plane. II. the planar, classical, two-dimensional magnet, J. Phys. France **36**, 581 (1975).

[58] G. Giachetti, N. Defenu, S. Ruffo, and A. Trombettoni, Villain model with long-range couplings, J. High Energy Phys. 02 (2023) 238.

[59] Y. V. Kovchegov and D. T. Son, Critical temperature of the deconfining phase transition in (2+1)d Georgi-Glashow model, J. High Energy Phys. 01 (2003) 050.

[60] L. Benfatto, C. Castellani, and T. Giamarchi, Berezinskii–Kosterlitz–Thouless transition within the sine-gordon approach: The role of the vortex-core energy, in *40 Years of Berezinskii–Kosterlitz–Thouless Theory* (World Scientific, 2013), Chap. 5, pp. 161–199.

[61] X. Jiao, W. Dong, M. Shi, H. Wang, C. Ding, Z. Wei, G. Gong, Y. Li, Y. Li, B. Zuo, J. Wang, D. Zhang, M. Pan, L. Wang, and Q.-K. Xue, Significantly enhanced superconductivity in monolayer FeSe films on $SrTiO_3$(001) via metallic δ-doping, Natl. Sci. Rev. **11**, nwad213 (2023).

[62] M. Gabay and A. Kapitulnik, Vortex-antivortex crystallization in thin superconducting and superfluid films, Phys. Rev. Lett. **71**, 2138 (1993).

[63] P. Minnhagen, The two-dimensional coulomb gas, vortex unbinding, and superfluid-superconducting films, Rev. Mod. Phys. **59**, 1001 (1987).

[64] T. Giamarchi and H. J. Schulz, Anderson localization and interactions in one-dimensional metals, Phys. Rev. B **37**, 325 (1988).

[65] T. Watashige, Y. Tsutsumi, T. Hanaguri, Y. Kohsaka, S. Kasahara, A. Furusaki, M. Sigrist, C. Meingast, T. Wolf, H. v. Löhneysen, T. Shibauchi, and Y. Matsuda, Evidence for time-reversal symmetry breaking of the superconducting state near twin-boundary interfaces in FeSe revealed by scanning tunneling spectroscopy, Phys. Rev. X **5**, 031022 (2015).

[66] N. Zaki, G. Gu, A. Tsvelik, C. Wu, and P. D. Johnson, Time-reversal symmetry breaking in the Fe-chalcogenide superconductors, Proc. Natl. Acad. Sci. USA **118**, e2007241118 (2021).

[67] Y. Dai, Z. Zhou, A. Ghosh, R. S. K. Mong, A. Kubo, C.-B. Huang, and H. Petek, Plasmonic topological quasiparticle on the nanometre and femtosecond scales, Nature (London) **588**, 616 (2020).

[68] R. P. Feynman, Slow electrons in a polar crystal, Phys. Rev. **97**, 660 (1955).

[69] P. L. Taylor and O. Heinonen, Electron–phonon interactions, in *A Quantum Approach to Condensed Matter Physics* (Cambridge University Press, 2002), pp. 210–231.

[70] F. Caruso and F. Giustino, Theory of electron-plasmon coupling in semiconductors, Phys. Rev. B **94**, 115208 (2016).

[71] The maximum value of 0.2 for g_{el-L} is chosen as it corresponds to the value of W_L, the variation of the magnetization energy with the local magnetization.

[72] From the polaronic model, this would correspond to the "Debye frequency," which in turn is expected to be close to the frequency of optical-like modes, such as the vortexes in this model. The value is again consistent with the dispersion observed for the magnetization energy of the SAFM phase in Fig. 2.

[73] S. L. Skornyakov, V. I. Anisimov, D. Vollhardt, and I. Leonov, Correlation strength, lifshitz transition, and the emergence of a two-dimensional to three-dimensional crossover in FeSe under pressure, Phys. Rev. B **97**, 115165 (2018).

[74] R. S. Kumar, Y. Zhang, S. Sinogeikin, Y. Xiao, S. Kumar, P. Chow, A. L. Cornelius, and C. Chen, Crystal and electronic structure of FeSe at high pressure and low temperature, J. Phys. Chem. B **114**, 12597 (2010).

[75] S. Margadonna, Y. Takabayashi, M. T. McDonald, K. Kasperkiewicz, Y. Mizuguchi, Y. Takano, A. N. Fitch, E. Suard, and K. Prassides, Crystal structure of the new $FeSe_{1-x}$ superconductor, Chem. Commun. 5607 (2008).

[76] Y. Mizuguchi, Y. Hara, K. Deguchi, S. Tsuda, T. Yamaguchi, K. Takeda, H. Kotegawa, H. Tou, and Y. Takano, Anion height dependence of T_c for the Fe-based superconductor, Supercond. Sci. Technol. **23**, 054013 (2010).

[77] T. Holstein and H. Primakoff, Field dependence of the intrinsic domain magnetization of a ferromagnet, Phys. Rev. **58**, 1098 (1940).

[78] G. Trimarchi, Z. Wang, and A. Zunger, Polymorphous band structure model of gapping in the antiferromagnetic and paramagnetic phases of the mott insulators MnO, FeO, CoO, and NiO, Phys. Rev. B **97**, 035107 (2018).

[79] A. Zunger, S.-H. Wei, L. G. Ferreira, and J. E. Bernard, Special quasirandom structures, Phys. Rev. Lett. **65**, 353 (1990).

[80] DOI:10.24435/materialscloud:md-y6.